

Review

Temperature Matters: Enhancing Performance and Stability of Perovskite Solar Cells through Advanced Annealing Methods

Shengcong Wu ^{1,2,3}, Chi Li ^{1,2,3} , Shui Yang Lien ⁴  and Peng Gao ^{1,2,3,*} 

¹ CAS Key Laboratory of Design and Assembly of Functional Nanostructures, and Fujian Provincial Key Laboratory of Nanomaterials, Fujian Institute of Research on the Structure of Matter, Chinese Academy of Sciences, Fuzhou 350002, China; lichil@fjirsm.ac.cn (C.L.)

² Laboratory for Advanced Functional Materials, Xiamen Center of Rare Earth Materials, Haixi Institute, Chinese Academy of Sciences, Xiamen 361021, China

³ University of Chinese Academy of Sciences, Beijing 100049, China

⁴ School of Opto-Electronic and Communication Engineering, Xiamen University of Technology, Xiamen 361024, China; syl@mail.dyu.edu.tw

* Correspondence: peng.gao@fjirsm.ac.cn

Abstract: Perovskite solar cells (PSCs) have garnered significant attention in the photovoltaic field owing to their exceptional photoelectric properties, including high light absorption, extensive carrier diffusion distance, and an adjustable band gap. Temperature is a crucial factor influencing both the preparation and performance of perovskite solar cells. The annealing temperature exerts a pronounced impact on the device structure, while the operational temperature influences carrier transport, perovskite band gap, and interface properties. This paper provides a comprehensive review of the influence of varied annealing temperatures on the hole transport layer, electron transport layer, and perovskite layer. Additionally, we present an overview of innovative annealing methods applied to perovskite materials. The effects of diverse working temperatures on the overall performance of perovskite cells are thoroughly examined and discussed in this review. In the end, different temperature conditions under ISOS testing conditions are summarized.

Keywords: temperature; annealing; perovskite; hole transport layer; electron transport layer; ISOS



Citation: Wu, S.; Li, C.; Lien, S.Y.; Gao, P. Temperature Matters: Enhancing Performance and Stability of Perovskite Solar Cells through Advanced Annealing Methods. *Chemistry* **2024**, *6*, 207–236. <https://doi.org/10.3390/chemistry6010010>

Academic Editor: Andrea Peluso

Received: 30 December 2023

Revised: 18 January 2024

Accepted: 23 January 2024

Published: 30 January 2024



Copyright: © 2024 by the authors. Licensee MDPI, Basel, Switzerland. This article is an open access article distributed under the terms and conditions of the Creative Commons Attribution (CC BY) license (<https://creativecommons.org/licenses/by/4.0/>).

1. Introduction

Solar energy represents a sustainable and environmentally friendly power source, with solar photovoltaic devices serving as instrumental tools for converting solar energy into electricity. Over the past decade, perovskite solar cells (PSCs) have undergone rapid development, capturing widespread attention and engendering substantial research interest within the global scientific community [1,2]. The exceptional properties of perovskite, including a broad light absorption range, extensive carrier diffusion length, and low exciton binding energy, underscore its potential for widespread application [3]. As the conversion rate of PSCs continues to advance, there is an optimistic anticipation of their large-scale commercial production. Some experts even project the feasibility of achieving mass production of perovskite photovoltaics by the year 2025 [4].

PSCs can be generally divided into two categories: flexible perovskite solar cells (FPSCs) and rigid perovskite solar cells. FPSCs usually use a polymer substrate (e.g., polyethylene 2, 6-naphthalene diformate (PEN), or polyethylene terephthalate (PET)), and these polymer substrates have poor stability at high temperatures. Therefore, FPSCs usually need to be prepared under low-temperature conditions, and the preparation temperature of TiO_x and NiO_x is relatively high, so FPSCs are not suitable for the high-temperature preparation step of such substances. In PSCs, the perovskite layer is sandwiched between the electron transport layer (ETL) and the hole transport layer (HTL). PSCs mainly have two different structural types: normal (n-i-p structure, including mesoscopic structure)

and inverted structure (p-i-n structure). Due to the high preparation temperature of mesoporous structures, they are generally not suitable for inverted structures. n-i-p-structured devices are constructed of transparent electrode/electron transport layer/mesoporous layer/perovskite layer/hole transport layer/counter electrode. The mesoporous layer is a scaffold, and perovskite material is filled in the mesoporous layer, which is responsible for assisting the separation of photogenerated carriers and avoiding direct contact between the HTL and the ETL. Sunlight passes through the transparent electrode and the ETL before it is absorbed by the perovskite film and finally converted into free carriers. The holes are transferred to the outer circuit along the HTL and the opposite electrode. Electrons are transferred to the external circuit along the electron transport layer and transparent electrode. In the planar structure, the perovskite film is deposited on the carrier transport layer, and direct contact is formed between the two functional layers, which simplifies the device preparation process.

In contrast to the normal planar structure, the inverted planar structure first deposits HTL on the substrate. p-i-n-structured devices are constructed of transparent electrode/HTL/perovskite layer/ETL/metal electrode. The perovskite film absorbs sunlight after passing through transparent electrodes and HTL and is finally converted into free carriers. The electrons and holes are transferred from the metal electrode and the transparent electrode to the external circuit, respectively.

Since normal PSCs have a different structure from the inverted PSCs, the ETL and HTL need to have different characteristics. The structure of PSCs as shown in Figure 1. For normal PSCs, since HTL is located on top of the perovskite layer, it needs to be highly hydrophobic. It can act as an effective protective layer for perovskite against moisture exposure. However, in inverted PSCs, HTL is deposited first. Then, perovskite is deposited on top of HTL, so HTL for inverted PSCs requires suitable surface wettability as a substrate for subsequent deposition and crystallization of perovskite [5]. In addition, since sunlight needs to pass through HTL first, the light transmissivity of HTL in inverted PSCs will also affect the light absorption efficiency of the perovskite layer [6]. In addition, the HTL thickness of inverted devices is always thin, so the requirement for hole mobility is not as high as that of conventional devices [7].

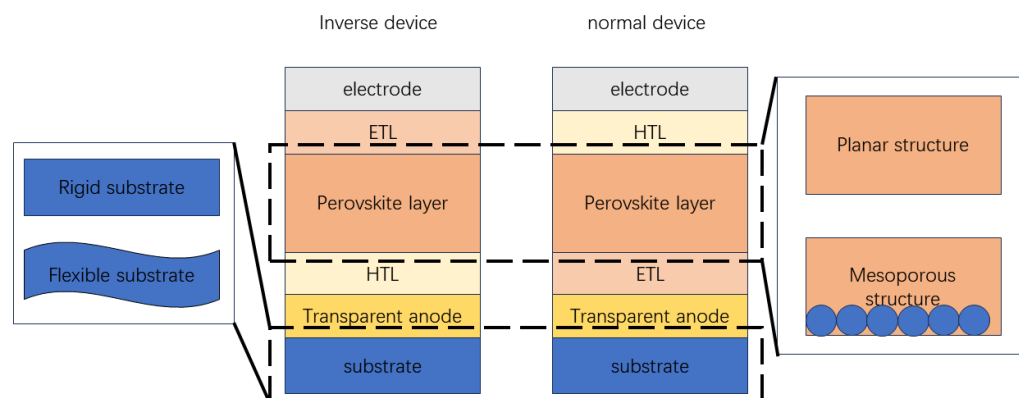


Figure 1. The structure of PSCs.

The fabrication of PSCs almost invariably involves high-temperature annealing [8,9]. This crucial step not only enhances film quality by increasing grain size, eliminating inter-grain cracks, and achieving a compact, smooth film but also boosts light absorption, reduces internal defects, and extends carrier lifetime. Consequently, annealing temperature emerges as a pivotal factor significantly influencing both the fabrication process and the performance of PSCs [10,11]. In summary, temperature exerts influence across various aspects: (i) concerning the electron transport layer (ETL), it accelerates crystallization, eliminates defects, and enhances substrate adhesion; (ii) alongside the conventional hotplate annealing method, new approaches such as rapid thermal annealing (RTA), intense pulsed light (IPL), liquid medium annealing (LMA), and post-annealing microwave treatment (MPAT) have

emerged; (iii) the actual operational environment, marked by fluctuating temperatures, significantly impacts the performance of photovoltaic devices, altering the band gap of the light-absorbing layer and influencing carrier transport at the interface. Additionally, the temperature coefficient (T.C.) of PSCs and ISOS test conditions are summarized in detail.

2. Temperature Control in Processing and Preparation

2.1. Electron Transport Layer

In this fast-developing field, the selection of ETLs has become significant. On the one hand, it is essential for charge transport and energy level matching. On the other hand, it is also significant for achieving high stability. TiO₂, ZnO, SnO₂, and PCBM are the most used ETL. ZnO, SnO₂, TiO₂ are often used for normal devices, and PCBM is often used for inverted devices.

2.1.1. TiO₂

The TiO₂ is generally used as the ETLs of PSCs, which guarantee electron injection from the perovskite layer to the ETL by direct contact, and its VBM is at a shallow position, which gives TiO₂ excellent hole-blocking properties. In addition, it is easy to control the morphology well, and its refractive index is low. There are many methods to prepare TiO₂ layers for PSCs, such as spin-coating (hydrolysis [12], nanoparticles [13]), spray pyrolysis [14], chemical bath deposition (CBD) [15], atomic layer deposition (ALD) [16], and electrochemical deposition [17].

There are three phases of TiO₂: anatase, rutile, and brookite [18], of which the structures are shown in Figure 2a–c. The band gap of rutile is 3.06 eV, while anatase TiO₂ is generally believed to have an absorption edge of about 3.2 eV. The band gap energy of brookite is between 3.1 and 3.4 eV [19]. The preparation of brookite is complex, so there are few studies about this phase. The anatase and rutile are the most valuable polymorphs of TiO₂; anatase is stable in low temperatures, and rutile is a steady phase at high temperatures [19]. The phase transition of TiO₂ is related to annealing time, heating rate, and temperature, and these factors can also affect the morphology of TiO₂. Because of the lower Gibbs free energy of the rutile phase, the rutile phase will transform into the anatase phase at reduced temperatures [20], and the phase transition from the rutile phase to the anatase phase is non-spontaneous. Some studies have shown that the anatase phase begins to transform from amorphous to crystalline below 280 °C [21], and the anatase phase transforms into a rutile crystalline phase above 700 °C [22]. Figure 2d shows the transformation mechanism from the anatase phase to the rutile phase. The phase transition mechanism is a core–shell reaction process. During the heating process, the phase transformation begins at the surface. With the extension of reaction time, the phase transition from anatase to rutile occurs from surface to interior [23].

Three phases of TiO₂ can be used as the ETLs of PSCs [24]. Hu et al. investigated a composite consisting of 1D cation-doped TiO₂ brookite nanorod (N.R.) embedded with 0D fullerene as ETL for inverted PSCs. Moreover, the transition metal Co or Fe cations were incorporated into brookite N.R. to adjust its electronic properties further. This kind of PSC has an efficiency of over 22% and a 22-fold increase in operating lifetime [25]. Kogo et al. prepared a highly crystalline layer of brookite using a sinter-free solution process as ETL. The nanoparticles formed by dehydration and condensation reaction formed a uniform mesoporous layer at low temperatures (130–150 °C). Compared with the anatase TiO₂ mesopore structure prepared by sintering at a high temperature (500 °C), the brookite electronic collector has a more significant fill factor (FF) and a higher photovoltaic performance of 100 mV open circuit voltage [26]. The efficiency of the device prepared using the three types of TiO₂ is shown in Table 1. Wang et al. fabricated PSC ETLs with rutile and anatase phase TiO₂. The results show that rutile ETL can enhance electron extraction and transfer and reduce electron binding due to its better electrical conductivity and improved interface with the MAPbI₃ (CH₃NH₃PbI₃) layer. Compared with anatase TiO₂ ETL, the PCE of MAPbI₃ PSCs containing a rutile TiO₂ ETL can reach up to 20.9%,

and the open circuit voltage (VOC) can reach up to 1.17 V [27]. Shahvaranfard et al. used single-crystalline rutile nanorod (N.R.) arrays as the ETL [28]. Under optimized conditions, a synergistic effect of the combined treatment was observed, resulting in a significant increase in cell efficiency, from 14.2% to 19.5%, and suppression of hysteresis. This cell shows JSC, VOC, and F.F. as high as 23.2 mA cm^{-2} , 1.1 V, and 77%.

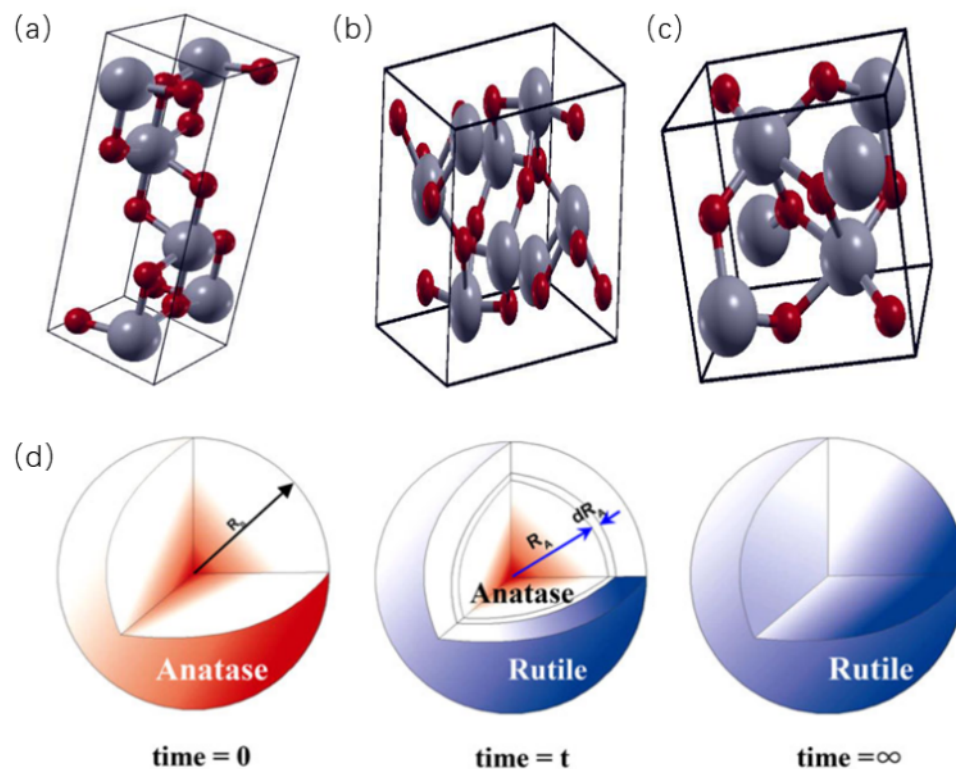


Figure 2. Three phases of TiO₂: (a) anatase, (b) rutile, and (c) brookite [18]. Copyright 2022, IOP publishing. (d) The transformation mechanism from the anatase phase to the rutile phase [23]. Copyright 2013, Springer Publishing.

Table 1. Photovoltaic performance of perovskite cells with brookite TiO₂ (non-sintered), anatase TiO₂ (sintered), and Al₂O₃ (sintered) layers. Data collected for each four cells [26].

Scan Direction	Mesoporous Layer	J _{SC} (mA cm ⁻²)	V _{OC} (V)	Fill Factor	PCE (%)
Forward	Brookite TiO ₂	20.2 ± 0.6	0.98 ± 0.01	0.69 ± 0.01	13.5 ± 0.6
−0.1 V					
↓ ^a	Anatase TiO ₂	19.4 ± 1.4	0.87 ± 0.01	0.62 ± 0.01	10.3 ± 0.7
1.1 V	Al ₂ O ₃	19.2 ± 1.3	1.05 ± 0.02	0.55 ± 0.03	11.0 ± 0.8
Backward	Brookite TiO ₂	20.0 ± 0.6	0.99 ± 0.01	0.67 ± 0.03	13.3 ± 1.0
1.1 V					
↓	Anatase TiO ₂	19.4 ± 1.4	0.90 ± 0.01	0.66 ± 0.01	11.5 ± 0.6
−0.1 V	Al ₂ O ₃	18.5 ± 1.6	1.05 ± 0.02	0.66 ± 0.05	12.7 ± 0.3

^a The arrow indicates the scanning direction of the voltage

Annealing temperature has a significant influence on the surface morphology of TiO₂. The SEM images are shown in Figure 3. When TiO₂ is placed at room temperature and annealed at 200, 400, and 600 °C, the particle size of TiO₂ gradually increases with the increase in annealing temperature.

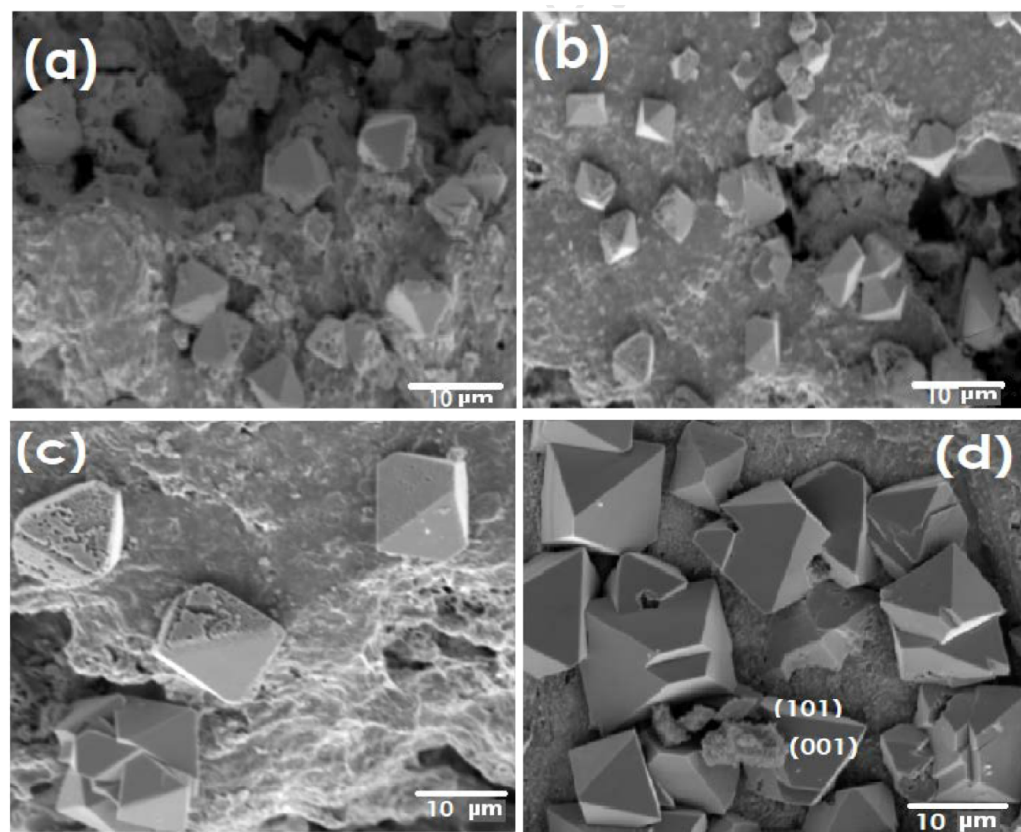


Figure 3. SEM micrographs of TiO₂ nanostructures (a) as-prepared and (b–d) annealed at 200, 400, and 600 °C, respectively [29]. Copyright 2018, ELSEVIER publishing.

It has been reported that the performance of solar cells relies heavily on the exposed crystal facet. Because the {001} anatase facets are the most exposed in single crystals, they are believed to have a good charge transfer potential [29]. Therefore, anatase TiO₂ is the most used electron transport layer in PSCs. Most TiO₂ films must be sintered at 500 °C to convert the amorphous oxide layer into crystalline form, which has specific conductivity and reasonable charge transport ability.

Hossain et al. deposited TiO₂ films on ITO glass substrate at room temperature (R.T., 25 °C) using an electron beam evaporation (EBE) system [30], as shown in Figure 4, and annealed TiO₂ films at different temperatures. The TiO₂ film prepared at R.T. shows an amorphous structure with a compact surface and Ti³⁺ state. Crystallinity and porosity of the TiO₂ films increase with the increase of annealing temperature. With the increase in annealing temperature, the grain boundaries of TiO₂ films gradually become clear, and the size and porosity of TiO₂ films gradually increase. Lv et al. applied the hydrothermal approach to grow highly oriented anatase TiO₂ nanopyramid arrays to be the ETL for PSCs [31]. They annealed TiO₂ film at 500 °C in a muffle furnace for 1 h to remove organic compounds. As a result, the anatase TiO₂ nanopyramid arrays-PSCs delivered a champion power conversion efficiency of ~22.5%.

However, high-temperature processes make the manufacturing process complicated and costly. Therefore, it is necessary to develop a low-temperature annealing ETL. For example, Kim et al. [32] first used ALD to prepare a TiO₂ compact film without annealing for flexible PSCs. Plasma-enhanced ALD can form a 20 nm thick dense layer of TiO_x on a plastic conductive substrate below 80 °C. They proposed highly bendable pero-SCs with a bending radius of 1 mm, while the devices with a bending radius of 10 mm can withstand up to 1000 cycles, maintaining more than 95% of the initial PCE. Liu et al. introduced a bi-functional molecule (thioacetamide, TAA) in TiO₂ ETL through low-temperature annealing (150 °C). The N and S atoms in TAA could bond with the Ti atom in the ETL and the Pb

atom in the perovskite layer, respectively [33]. Therefore, the formation of coordinate bonds was good for increasing crystallinity and reducing the roughness of TiO₂ ETLs and PVK layers, which could effectively passivate defects. Based on the surface spin-coated TAA TiO₂ ETL, the PSC achieved the best power conversion efficiency (PCE) of 21.17%. Hsu et al. prepared dense tantalum-doped titanium oxide films as the ETL of PSCs [33]. The effects of ta-doped TiO₂ on the structure and electronic properties of the films and the effects of different annealing temperatures on the properties of the films were studied. The results of refractive index spectrum, X-ray diffraction (XRD), X-ray photoelectron spectroscopy (XPS), and photoluminescence (PL) explain the effects of different annealing temperatures on the film quality, including the doping of Ta atom TiO₂ film and the introduction of annealing treatment to reduce film defects. XPS results showed Ta ion incorporation. The resistivity of doped Ta films is orders of magnitude lower than that of undoped TiO₂ films. The results of XPS show that TiO₂ ETL doped with Ta after annealing has fewer structural defects. The annealing process can passivate defects and improve film quality. Finally, using Ta doping and 400 °C annealing treatment, the maximum F.F. of Ta-doped TiO₂ ETL PSCs was 0.77, and the power conversion efficiency (PCE) was 19.62%, higher than that of undoped TiO₂ ETLs.

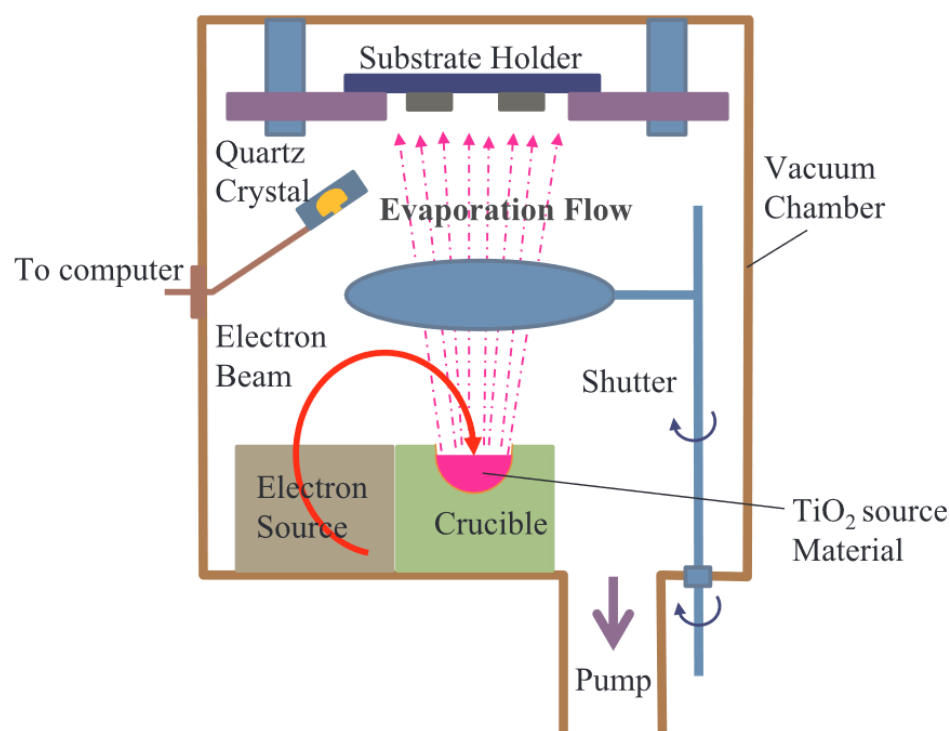


Figure 4. The schematic diagram of the E-beam evaporation system [30]. Copyright 2018, Springer Publishing.

2.1.2. ZnO

ZnO is a widely used ETL material that has attracted much attention. ZnO is a semiconductor material with a direct band gap (3.11–3.36 eV) with an exciton binding energy of 60 meV. Compared with TiO₂, ZnO has higher electron mobility and lower growth temperature. In addition, ZnO-based PSCs are superior in fulfilling application demands owing to their relatively lower cost, more straightforward deposition process, milder sintering temperatures, and higher electron mobility (~200 cm²/Vs). It is stable, low in price, provides environmental protection, and has other chemical characteristics. Since ZnO is almost soluble in water, it is often used for solution-based processing at lower temperatures. Its appearance is a white to yellowish-white crystalline substance. There are three forms of ZnO: cubic zinc blende, hexagonal wurtzite, and cubic rock salt [34]. The various crystal structures of ZnO are shown in Figure 5.

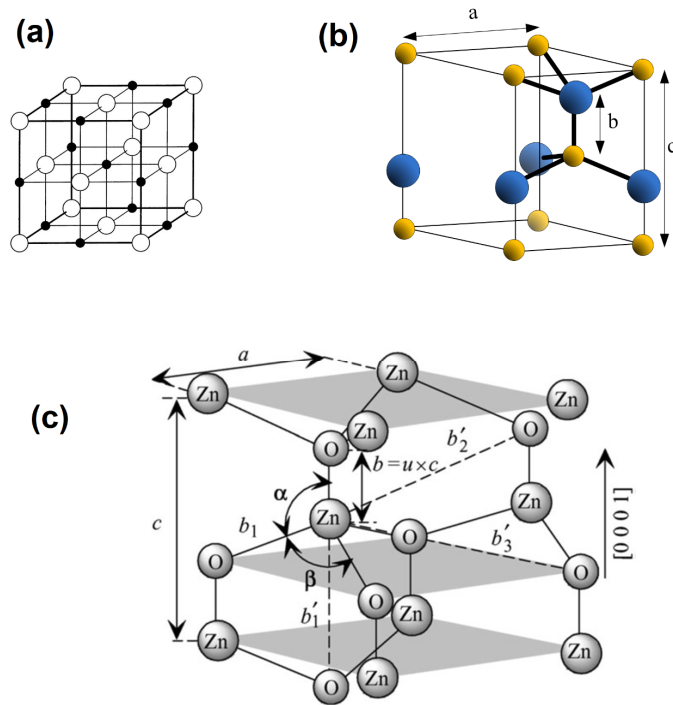


Figure 5. Structures of ZnO. In (a), cubic rock salt; in (b), wurtzite hexagonal; and in (c), the wurtzite lattice constants a–c [34]. Copyright 2022, MDPI publishing.

The hexagonal wurtzite crystal structure shown in a and b in Figure 6 is stable at room temperature and atmospheric pressure, and the cubic martensite is formed under high pressure [35]. In general, ZnO has several high-speed growth directions: $\pm [2\bar{1}\bar{1}0]$, $\pm [1\bar{2}\bar{1}0]$, $\pm [1\bar{1}\bar{2}0]$, $\pm [0\bar{1}\bar{1}0]$, $\pm [10\bar{1}0]$, $\pm [1\bar{1}00]$, and $\pm [0001]$ [36]. By adjusting the growth rate in these directions, a variety of different morphologies can be obtained, such as one-dimensional (1D), two-dimensional (2D), and three-dimensional (3D), as shown in Figure 6. This highlights the diversity of ZnO morphological structures.

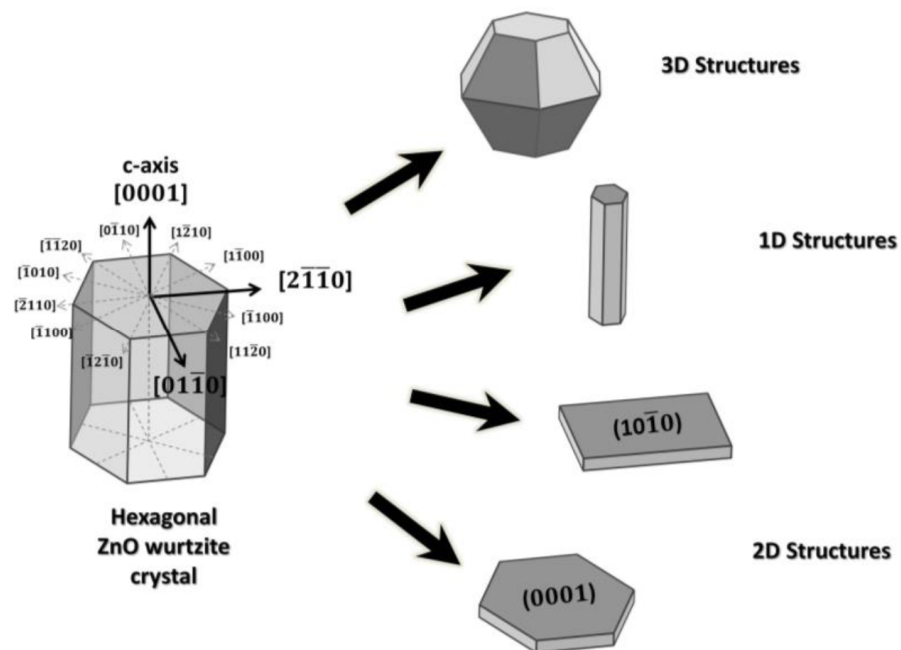


Figure 6. Preferential growth directions of ZnO wurtzite crystal and possible structures [37]. Copyright 2017, MDPI publishing.

In PSC, ZnO and MAPbI₃ layers are composed of corresponding nanoparticles. In this structure, the interface between ZnO and MAPbI₃ can be manufactured along an orientation relationship (OR). Li [38] used the modified phenomenological theory of Martensitic crystallography and first-principles calculations to analyze the atomic system of the surface between ZnO and MAPbI₃. Based on the interface energy, they found that ZnO nanoparticles are loosely positioned on the MAPbI₃ substrate under equilibrium conditions. From the morphology perspective, ZnO prepared at low temperatures deviate from the equilibrium shape [39,40], which may contribute to improving the efficiency of PSCs. With the increase in temperature, ZnO nanoparticles gradually transform into an equilibrium state, destroying the stability of PSCs. Therefore, low-temperature processes are often adopted when using ZnO as the ETL.

Figure 7a shows the surface morphology of ZnO films using atomic force microscopy. The surface morphology of ZnO films presents a uniform granular morphology at different annealing temperatures, and there are some columnar grains. When the annealing temperature is less than 400 °C, the roughness increases with the increase in annealing temperature. The roughness decreases with the increase in annealing temperature. Figure 7b is the SEM image. The surface of ZnO becomes smooth when the temperature is higher than 80 °C.

The properties of ZnO prepared by different synthesis methods are also different. There are several methods to prepare ZnO. Adnan et al. used the sol-gel method to prepare ZnO [41]. They investigated the electrical and optical properties of ZnO electron transport layer-based PSCs. This synthesis protocol provides a relatively cheaper and faster method of fabrication of solar cells. Niu et al. prepared the ZnO ETL using a vacuum-based magnetron sputtering method [42]. This method can efficiently diminish the defect of the ZnO surface. Yun et al. prepared a vertical ZnO nanorod at low temperatures [43]. ZnO grown on FTO can be effectively regulated by controlling the reaction time. They prepared the high-performance mesoporous PSCs by using the vertical ZnO nanorod. Yang et al. prepared ZnO by a one-step method, modified with three amino compounds: butylamine (B.A.), isobutylamine (IBA), and 2-amino-2-methyl-1-propanol (AMP), which improved the conductivity of ZnO and formed a more stable perovskite on ZnO.

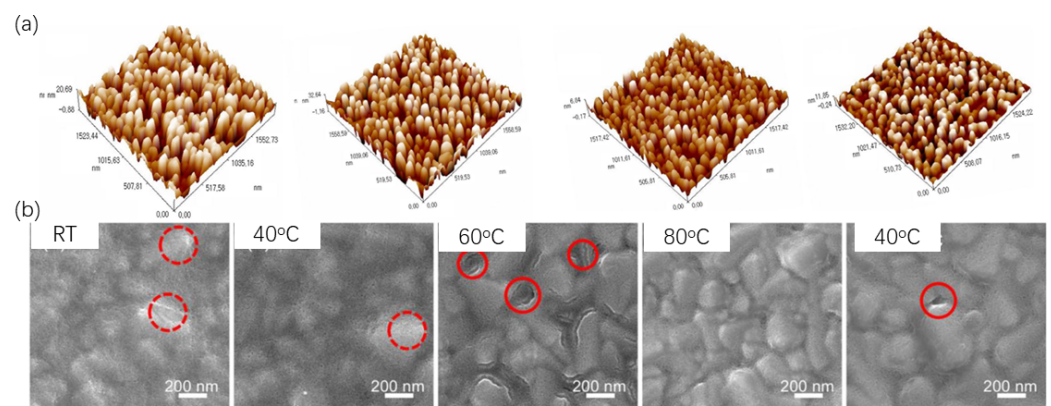


Figure 7. (a) AFM images of ZnO thin films as-deposited and annealed at 400 °C, 500 °C, and 600 °C (from left to right) [44]. Copyright 2022, AMER INST PHYSICS publishing. (b) SEM images of slot-die coated ZnO on FTO with the substrate temperature at room temperature, 40, 60, 80, and 100 °C, The red circle indicates a crack [45]. Copyright 2021, ELSEVIER SCI LTD publishing.

2.1.3. SnO₂

SnO₂ is an efficient ETL material with excellent bulk electron mobility, deep conduction bands, and good energy levels. SnO₂ exhibits excellent chemical stability, U.V. resistance, good antireflection, and less photocatalytic activity. In addition, SnO₂ has a small refractive index and wide optical band gap (3.6–4.0 eV), resulting in high transmittance across the entire visible spectrum [46]. SnO₂ compact ETLs were prepared through a simple sol-gel

technique and used for the first time as an ETL in PSCs by Dong et al. in 2015 [47], the sintering process in a furnace at 450 °C. The best PCE is 9.83%.

A SnO₂ ETL is often prepared using the low-temperature method because annealing under high-temperature conditions causes a decline in the performance of the SnO₂, resulting in the performance and stability of the device and mismatched energy level with the adjacent perovskite layer [48]. It has been reported in multiple studies that the annealing temperature for preparing SnO₂ ETL is 180–200 °C. The SEM top view of SnO₂ after low- and high-temperature treatment is shown in Figure 8. The results show that although the crystallinity of SnO₂ at high temperatures is good, the film is not dense enough to plug the holes effectively, leading to more severe interface recombination and shunt path [49]. Wang et al. prepared SnO₂ thin film as the electron transport layer of perovskite cells using the low-temperature solution method [50]. They studied the influence of the annealing temperature of SnO₂ on the microstructure, the physical properties of the electron transport layer, and the performance of PSCs. The test results are shown in the figure below. According to the study about optics, electricity, and surface morphology, it is concluded that the optimal annealing temperature of SnO₂ as an electron transport layer is 180 °C. Ke et al. studied the morphology characteristics of SnO₂ treated at high and low temperatures [49]. SEM in Figure 8a,b shows that the SnO₂ nanoparticles annealed at low temperature (L.T.) can uniformly cover the FTO substrate, while the SnO₂ nanoparticles treated at high temperature (H.T.) will severely agglomerate, leaving many FTO regions not covered by SnO₂. Figure 8c,d shows that the LT-SnO₂ film is more smooth than the HT-SnO₂ film; therefore, the HT-SnO₂ film is not dense and cannot effectively plug holes, resulting in severe interfacial recombination and shunt paths.

There are some different deposition techniques to prepare the SnO₂ layer. The deposition techniques can be classified into two groups [51]: (1) physical deposition, such as sputtering and thermal evaporation, and (2) chemical deposition, such as sol–gel, atomic layer deposition (ALD), and chemical bathing deposition (CBD). The sol–gel method is the most widely used method to prepare SnO₂ layers in PSCs. Wang et al. put the pore-forming agent polyethylene glycol (PEG) into the nano SnO₂ colloidal precursor solution to deposition m-SnO₂ layer [52]. The precursor was spin-coated on the ITO glass substrate with a pre-deposited thin and dense SnO₂ barrier layer. LTP treatment was performed on the coated film to remove PEG in the film. Finally, a PEG mesoporous structure was formed in the membrane. Jia et al. used the combustion method to deposit a high-performance SnO₂ ETL [53]. Compared with the traditional solution treatment method, the SnO₂ layer prepared using the combustion method has better electron transport performance. The power conversion efficiency of the SnO₂ device using combustion method is 19.12%, which is higher than that of the traditional SnO₂ device.

However, the required manufacturing temperatures are still high and incompatible with most plastic substrates. To solve this problem, the researchers developed other annealing methods to promote the formation of metallic oxide layers at low temperatures. Liu et al. first regulated the electrical properties of SnO₂ by doping Nb⁵⁺ in SnO₂ sol–gel at low temperatures [54] (<100 °C), and the device efficiency increased from 18.06% to 19.38%. It provides a practical reference for preparing high-efficiency PSCs at low temperatures (<100 °C). Sun et al. prepared the electron transport layer of SnO₂ at room temperature by electrochemical deposition [55] and regulated the energy level of SnO₂ by adjusting the pH of the electrolyte. The optimal performance of the prepared device reached 22.85% efficiency, and the preparation process is shown in Figure 8e.

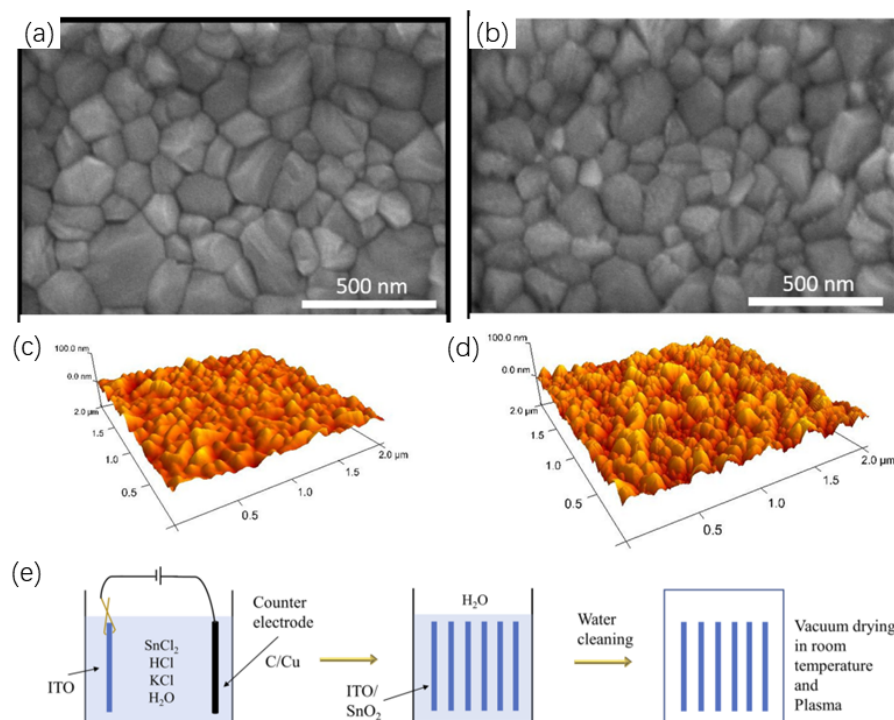


Figure 8. Top-view SEM images of 320 nm thick vacuum-processed perovskite films on (a) LT-SnO₂ and (b) HT-SnO₂ ESLs deposited on FTO substrates. AFM images of (c) LT- and (d) HT-SnO₂ thin films (40 nm) deposited on FTO substrates [49]. Copyright 2015, The Royal Society of Chemistry publishing. (e) Preparation process of SnO₂ (from left to right: depositing SnO₂, soaking to remove residues, vacuum drying, and plasma treatment) by electrochemical deposition [55]. Copyright 2023, The Royal Society of Chemistry publishing.

2.1.4. PCBM

Phenyl-C61-methyl butyrate (PCBM) is one of the most used ETL materials in inverted PSCs. PCBM is considered to be a good electron acceptor (Lewis acid) and is inactive to the perovskite layer [56]. PCBM was first used to invert PSCs in 2013 [57]. Lam et al. used PCBM as an ETL to understand the high performance of MAPbI₃ solar cells [58]. It was found that PCBM plays a decisive role in inhibiting halide ion migration in the perovskite layer through halide- π non-covalent interaction. This interaction increases electron transport in the ETL [59].

Huang et al. reported for the first time the use of PCBM to suppress the hysteresis of solar cells. They found that heat treatment of PCBM had a crucial effect on the performance of inverted PSCs, as the short circuit current density (J_{sc}) and FF increased after heat treatment. This is because heat treatment can enhance the diffusion of PCBM by breaking down the grain boundaries of the perovskite layer [60]. Choi et al. tested the SEM images of unannealed and annealed PCBM ETL [61], as shown in Figure 9. Figure 9a,b show cross-sectional SEM images of annealed and unannealed samples. The slight change in PCBM ETL thickness may be caused by the dense accumulation of PCBM molecules after annealing. Figure 9c,d show top-view SEM images of the sample, and no significant changes are observed. Therefore, annealing has no obvious effect on the morphology of the PCBM layer. Mehdi et al. tested the ultraviolet-visible absorption spectra and PL spectra of PCBM devices under different annealing times, as shown in Figure 9e,f [62]. It can be seen from Figure 9e that the absorption spectral shape of all perovskite films is the same; however, in the 300–500 nm range, after annealing for 10 min, the absorption intensity is slightly improved, which may be the result of enhanced light scattering caused by smooth and dense perovskite films. Figure 9f shows the PL spectra of ITO/PEDOT/perovskite/PCBM films at an excitation wavelength of 500 nm. With the extension of annealing time of PCBM,

PL strength decreases significantly, which indicates that annealing is beneficial to defect passivation and thus reduces charge recombination. Shao et al. tested the devices that did not contain PCBM and annealed PCBM at 100 °C for 15 min and 45 min, respectively [60]; after adding a layer of PCBM on the perovskite layer, the photocurrent lag decreases and disappears completely after annealing for 45 min.

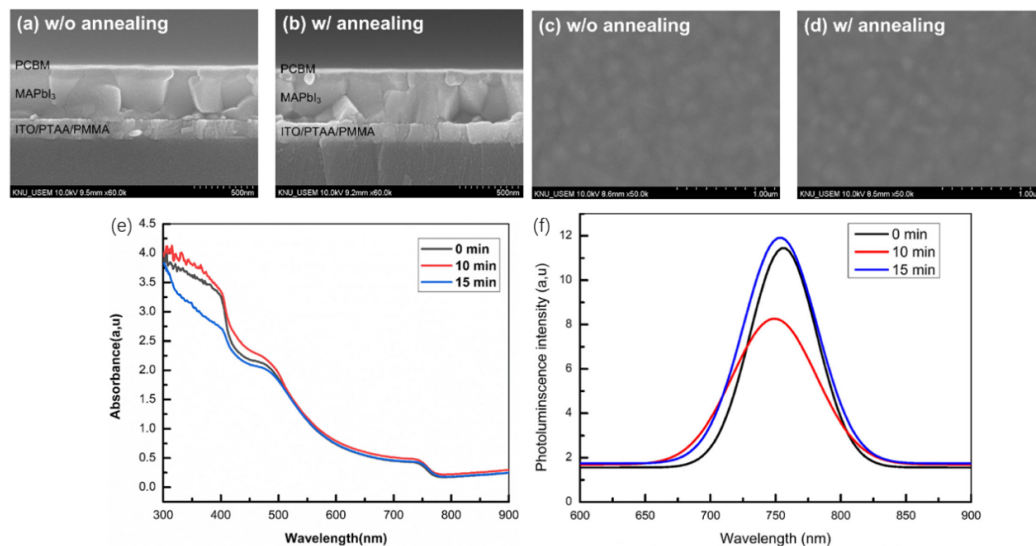


Figure 9. Cross-sectional view and top-view SEM images of ITO/PTAA/PMMA/MAPbI₃/PCBM (a,c) without annealing, and (b,d) with annealing [61]. Copyright 2022, Springer publishing. (e) Ultraviolet-visible absorption spectra and (f) PL spectra of ITO/PEDOT:PSS/MAPbI₃-xCl_x/PCBM with different annealing times of the PCBM [62]. Copyright 2022, Springer publishing.

In addition to the conventional annealing method (CA), where annealing of PCBM and perovskite are separated, the perovskite layer and PCBM can be simultaneously annealed, called the combined annealing method (MA), as shown in Figure 10a. Liu et al. prepared a batch of devices using the MA method [63]. The SEM and AFM of these devices are shown in Figure 10b–e. Compared with CA perovskite films, the crystallinity and grain size of MA films are significantly improved. Notably, monocrystalline perovskite particles were observed in cross-sectional SEM images of MA films. As shown in Figure 10d,e, unlike the small grains of CA film, which are unclear and different in size, MA film presents uniform monocrystalline perovskite grains, most of which are close to the top layer of PCBM/Al from the bottom electrode. This can effectively extract the charge at the electrode via direct transport channels in the perovskite crystals and significantly reduce the grain boundaries longitudinally. Wu et al. used transient photovoltage (TPV) measurements to study the charge recombination dynamics inside devices [64]. As shown in Figure 10f, MA-based devices have a longer attenuation lifetime compared to CA-based devices, indicating slower recombination kinetics and less energy loss due to the passivation of interface defects [65]. This indicates that the MA process and its merging interface can inhibit charge recombination and reduce energy loss, which is conducive to the increase in Voc. Zhou et al. dissolved PCBM in the anti-solvent CB to control the content of PCBM and dropped the solution on the surface of perovskite during the spin coating process. The J–V curve is shown in Figure 10g [66].

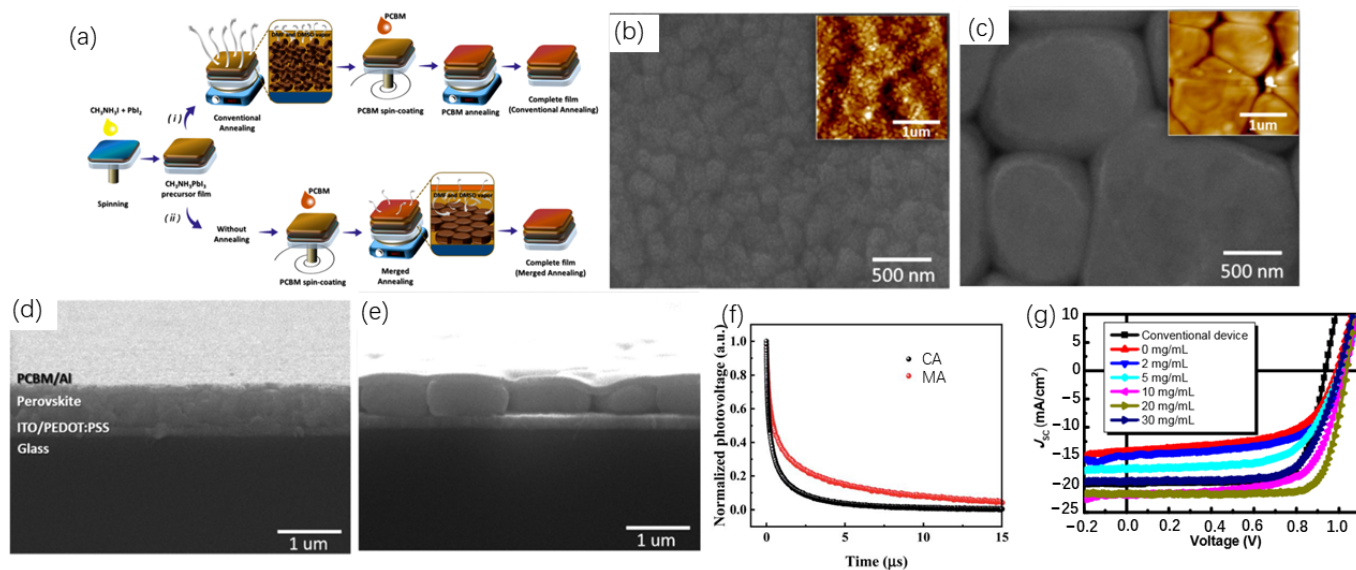


Figure 10. (a) Schematics of the conventional thermal annealing (CA) and merged annealing (MA) fabrication processes. SEM and AFM (inset) images of perovskite films fabricated by (b) CA and (c) MA. Cross-sectional SEM images of perovskite films fabricated by (d) CA and (e) MA [63]. Copyright 2017, ACS publishing. (f) TPV decay curves of the devices fabricated using CA and PMA processes [64]. Copyright 2021, RSC publishing. (g) J–V characteristics of MAPbI₃-xCl_x PSCs for conventional device and one-step method based on different contents of PCBM under the simulated AM 1.5G illumination of 100 mW/cm² [66]. Copyright 2016, RSC publishing.

2.2. Hole Transport Layer

The role of the hole transport layer is to transport holes to the TCO. Therefore, hole transport layer (HTL) materials should have high hole mobility and be able to block electrons. The hole transport layer should also have a certain degree of stability, not readily react with adjacent layers, and not quickly decompose under wet and high-temperature conditions. To save the cost of preparing PSCs entirely, studying HTL materials that can be prepared at lower temperatures is necessary. Materials commonly used as hole transport layers include spiro-OMeTAD, PTAA [67], PEDOT:PSS, and NiOx.

2.2.1. NiOx

NiO is a direct bandgap inorganic material with a band gap range of 3.6–4.0 eV and a work function of 5.4 eV [68]. It has the characteristics of high light transmission and electron blocking and should have good ohmic contact with the electrode. NiO also has good thermal stability, reasonable price, and abundant reserves and is often used for inverted PSCs. Studies have found that inorganic materials have good stability, carrier mobility, and lower cost. There are many preparation methods for NiO.

Jimenze et al. prepared NiO films by dip-coating sol-gel. They investigate the effect of annealing temperature on the crystal structure. It showed that the film is amorphous when annealed at 175–250 °C, and NiO is crystalline when annealed above 250 °C [69]. The annealing temperature has a specific effect on the surface morphology and crystal structure of NiO. At an annealing temperature of 300 °C, the crystal structure is amorphous, and its surface morphology of NiO is uneven. When the annealing temperature is higher than 300 °C, the surface of NiO becomes flat, and a regular crystal structure appears. The annealing temperature also impacts the refractive index and extinction coefficient of NiO [70]. Patil et al. found that when the annealing temperature of NiO film gradually increased from 400 °C to 700 °C, the band gap energy reduced from 3.86 eV to 3.47 eV, and the conductivity raised from 10⁻⁴ to 10⁻² (Ω·cm)⁻¹ [71]. In the range of 400–700 °C, with the growth in temperature, the average grain size is larger, causing the grain boundary density to decline and the carrier scattering to reduce. With the increase in annealing temperature,

the absorption coefficient of the film also increases because of the increased state density of the hole [72]. Thermal analysis shows that substances in NiO decompose below 400 °C, and after reaching 400 °C, the weight tends to stabilize, and NiO crystals are formed [73]. Kayani et al. investigated the change of NiO film when the annealing temperature was raised from 400 °C to 1000 °C. In the range of 400–1000 °C, with the increase in annealing temperature, the crystal size increases, the dislocation density gradually decreases, the transmittance also decreases with the increase in annealing temperature, and the band gap increases from 3.02 eV to 3.14 eV [74].

There are many methods to deposit NiO films in PSCs, including evaporation, sputtering, pulsed laser deposition (PLD), atomic layer deposition (ALD), the sol–gel method, spin-coating of pre-synthesized nanocrystals, and electrodeposition. Figure 11 illustrates several different synthesis methods [75].

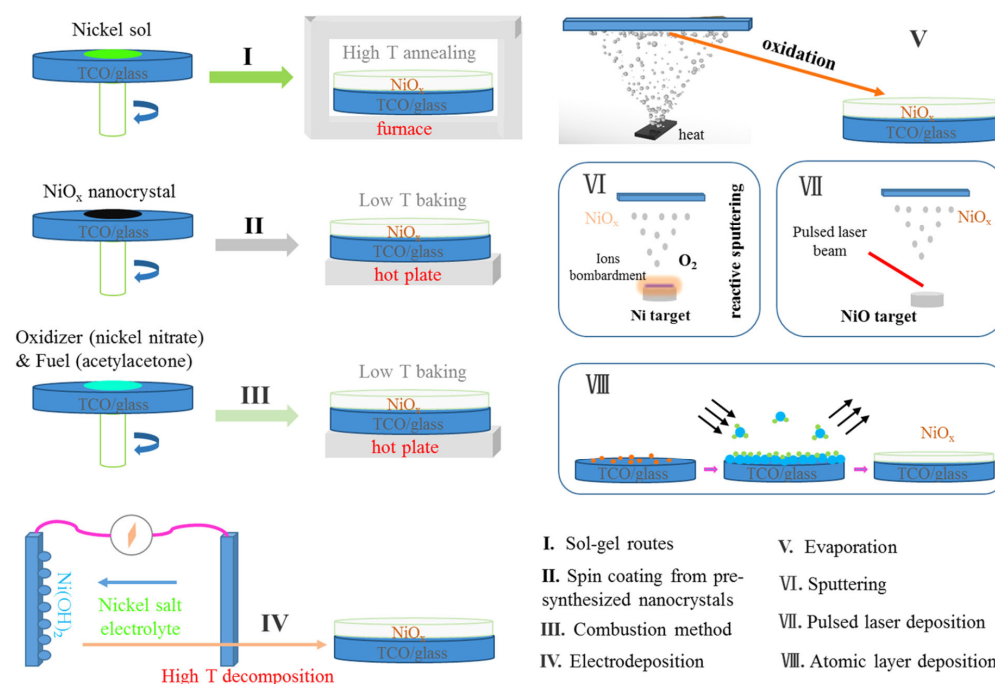


Figure 11. A schematic figure shows the different methodologies for depositing NiOx thin films [75]. Copyright 2019, Wiley Online Library publishing.

Different synthesis methods have different requirements for annealing temperature. For most preparation methods, such as the solution–gel method, NiO films are deposited by spin-coating or spray pyrolysis. After spin-coating, NiO is often annealed above 300 °C to eliminate organic impurities and crystallize the film. For spray pyrolysis, the substrate is usually heated to the required temperature, and the NiO is directly crystallized after being deposited on the substrate. Moreover, the crystallinity of NiO can also be improved by annealing treatment. NiO films can also be deposited by spin-coating of pre-synthesized nanocrystal suspensions. This method allows for the NiO film to crystallize in the spin-coating process, so there is no need for annealing at high temperatures, only a lower temperature post-heat treatment process to remove the organic components. Combustion is often used to deposit NiO films at relatively low temperatures. In the combustion reaction process, heat is quickly lost due to the large ratio of surface area to the volume of the film. There is little thermal effect on the underlying substrate, so this method can use a flexible plastic substrate. Electrodeposition is an economical and convenient method for preparing NiO thin films. The electrodeposition method usually involves depositing Ni(OH)₂ film by electrodeposition and then decomposing Ni(OH)₂ into NiO by annealing, during which the temperature is usually higher than 300 °C [76].

2.2.2. Polymer Material

Currently, the commonly used polymer HTL for inverted PSCs is PTAA, and spiro-OMeTAD is often used in normal PSCs. Polymer-based PSCs can be prepared at relatively lower temperatures than conventional PSCs.

Spiro-OMeTAD was first applied to the hole transport layer of PSCs in 2012, providing significantly improved stability compared to liquid junction PSCs [77]. Many devices that have set PSC efficiency records have used Spiro-OMeTAD as the hole transport layer [78]. Spiro-OMeTAD is easy to process, matches the common perovskite absorption layer level, and has good hole conductivity. A smooth, uniform, and pinhole-free Spiro-OMeTAD can be obtained using solvents such as chloroform, which is conducive to improving its overall performance. The glass transition temperature of Spiro-OMeTAD is approximately 125 °C [79]. Using dopants such as TBP and Li-TFSI can enhance the electrical conductivity and reduce this temperature to below 100 °C [80].

Although spiro-OMeTAD doping tBP and other p-type dopants can obtain higher efficiency, they have higher requirements for thermal stability [81]. Although pure spiro-OMeTAD has a high melting point, it is easy to crystallize under thermal stress of 100 °C, which has an adverse effect on the interface contact of spiro-OMeTAD [82]. Using the doped spiro-OMeTAD as the hole transport layer of the perovskite cell, spiro-OMeTAD is rapidly destroyed at 85 °C. At the same time, other structures in the device remain stable in this condition [81]. Mesquita et al. observed that after placing spiro-OMeTAD at high temperature for a while, the device performance would recover to a certain extent when tested at low temperature, suggesting that part of the decomposition process was reversible, as shown in Figure 12 [83]. The undoped spiro-OMeTAD at 80 °C had little influence. Thus, permanent degradation may be due to the evaporation of the dopant. Under 85 °C, tBP evaporates directly from the spiro-OMeTAD film [84], forming pinholes and causing rapid deterioration in device performance [85]. In addition, with the increase in temperature, the evaporation rate of tBP and the decomposition rate of spiro-OMeTAD also increase [86].

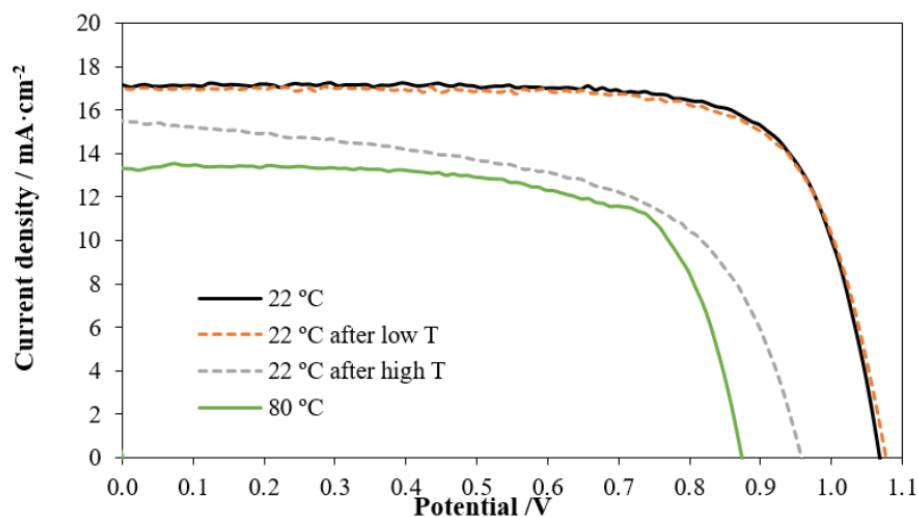


Figure 12. I–V curves of PSCs employing LiTFSI- and tBP-doped spiro-OMeTAD operating at various temperatures [83]. Copyright 2019, Wiley Publishing.

PTAA does not refer specifically to trimethyl-substituted poly (bis(4-phenyl)(2,4,6-trimethylphenyl) amines but rather broadly describes the kind of Poly-triphenylamine, an organic polymer semiconductor. In 2013, Heo et al. [87] applied PTAA as HTL to n-i-p structure PSCs for the first time. PTAA is soluble in most organic solvents, has a good energy level that matches the standard perovskite absorption layer, and has a stronger interaction with perovskite at the interface than other polymer semiconductors, which is conducive to hole transport. In addition, PTAA has a higher melting and glass transition temperature than spiro-OMeTAD, so PTAA has a higher thermal stability than

spiro-OMeTAD. It was found that PTAA is entirely amorphous. No glass transition or melt phase characteristics were observed in DSC analysis at up to 300 °C [88], and exceptionally smooth films were formed. At present, PTAA is often used as a hole transport layer for high-efficiency devices.

2.3. Perovskite Layer

In organic and inorganic metal perovskite halide ABX_3 , A represents a valence organic or inorganic cation, such as formamidinium ion ($HC(NH_2)_2^+$), ammonium ($CH_3NH_3^+$), cesium ion (Cs^+), rubidium ion (Rb^+), or a variety of cations mixed; B represents divalent metal cations, such as lead ion (Pb^{2+}), tin ion (Sn^{2+}), germanium ion (Ge^{2+}), or a mixture of metal ions, etc. X represents a single halogen anion, such as bromine ion (Br^-), iodide ion (I^-), chloride ion (Cl^-), or a mixture of halogen ions. The crystal structure of ABX_3 is shown in Figure 13. One metal B atom is coordinated with six halogen X atoms to form a $[BX_6]$ octahedral structure. Atom A is surrounded by eight octahedral skeletons sharing vertices, keeping the structure stable under the weak van der Waals force interaction.

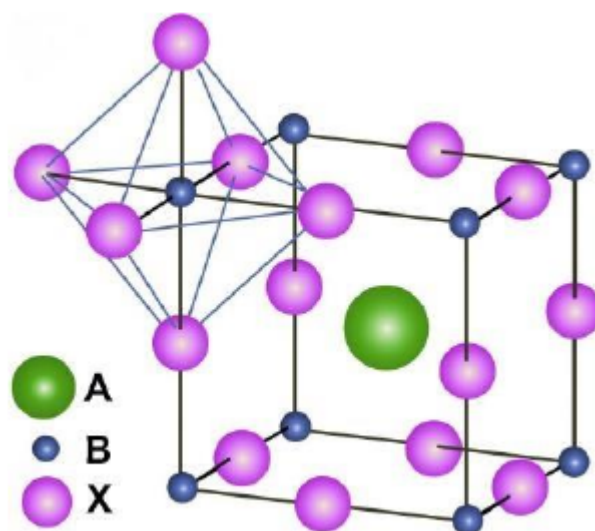


Figure 13. Crystal structure of perovskite [89]. Copyright 2020, ScienceDirect publishing.

The perovskite absorbent layer is an essential part of the whole PSC. The quality of perovskite film will significantly affect the performance during the period. The quality of the film is affected by crystallization, grain size, preparation temperature, defect density, and chemical composition, and thus determines the PCE and stability of the final PSCs. Because the optical and electrical properties of the perovskite layer are closely related to the film preparation technology, the research and development of the preparation technology of the perovskite layer have been widely considered by scientists in various countries and a great deal of energy has been put into them.

2.3.1. Effect of Annealing Temperature on Perovskite Material

The crystallization process of perovskite is an essential factor affecting the quality of the film, and the film preparation temperature plays a crucial role in the crystallization, nucleation, and growth process of perovskite. Researchers have carried out much work on the preparation temperature of the film. The perovskite solution, which is still in the solution state after the spin coating, contains a complex internal crystalline phase regulated by the intermediate phase of the polar solvent [90,91]. In addition to regulating the crystal structure of perovskite, annealing can also evaporate the solution and promote the transformation of perovskite mesophase into pure α phase [92]. GIWAXS results in Figure 14a show that $CH_3NH_3PbI_{3-x}Cl_x$ perovskite gradually transforms from the intermediate phase to the perovskite α phase during heat treatment [92]. At the beginning of annealing, the

peak of precursor mesophase is mainly in the solution. With the annealing of perovskite, the peak of mesophase gradually disappears, the diffraction peak of the perovskite α phase gradually increases, and the crystal orientation is obvious. Oyewole et al. used scanning electron microscopy to test the surface morphologies annealed at different temperatures, as shown in Figure 14b [93], and the test results clearly showed that the annealing temperature would significantly affect the surface morphologies of perovskite films. The grain size of the perovskite film annealed at 100 °C is small, and the grain size increases with the gradual increase in temperature. When the annealing temperature reaches 140 °C, the perovskite appears as sheet grain. The resulting films are coarser and have larger grain sizes than the low-temperature annealed perovskite films. The perovskite film annealed at 150 °C forms larger grains with gaps between the grains, exposing the underlying TiO₂ layer. Kazemi et al. used the time-correlated single photon counting (TCSPC) technique to study the radiation recombination dynamics of perovskite with annealing temperature, as shown in Figure 14c [94]. Therefore, the annealing temperature affects the performance of perovskite devices, as shown in Figure 14d [93].

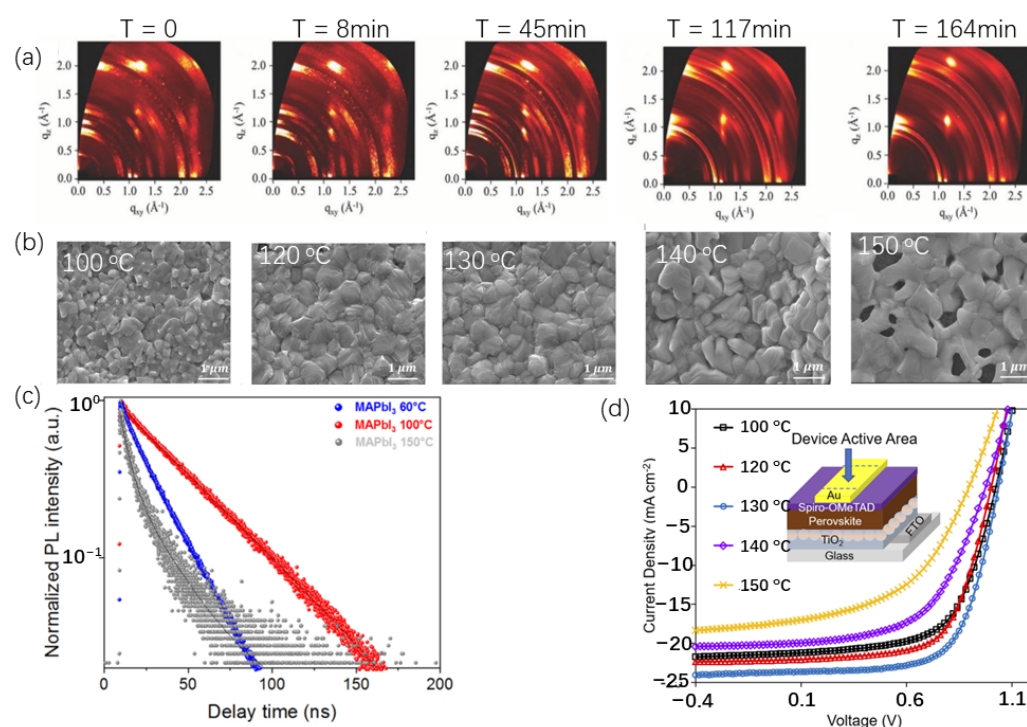


Figure 14. (a) Two-dimensional GIWAXS patterns recorded during annealing at 80 °C; images were captured at T = 0, T = 8 min, T = 8 min, T = 45 min, T = 117 min, and T = 164 min [92]. Copyright 2016, Wiley Online Library publishing. (b) SEM images of perovskite films annealed at 100 °C, 120 °C, 130 °C, 140 °C, and 150 °C [93]. Copyright 2021, AMER INST PHYSICS publishing. (c) Evolution of P.L. decay measured using time-correlated single photon counting (TCSPC) technique using 475 nm excitation (2 MHz, 100 nJ cm⁻² fluence), 775 nm emission (slit opening 10 nm) with a 645 nm long-pass filter for MAPbI₃ prepared at 60 °C, 100 °C, and 150 °C [94]. Copyright 2021, Frontiers Media S.A. publishing. (d) Current density–voltage curves of perovskite solar cells that were annealed at different temperatures (the inset is the schematic of the device structure, indicating the device active area) [93]. Copyright 2021, AMER INST PHYSICS publishing.

Mohammad et al. led a study using the temperature of MAPbI₃ crystallization as free parameters to investigate how they affect film properties and how device performance values are affected [94]. The results show that the crystallinity level of the grain is significant to the photocurrent value. At the same time, the morphology and PbI₂ impurity caused by the thermal decomposition of MAPbI₃ has adverse effects on the photovoltage and the filling factor value of the photovoltaic device. On this basis, it is emphasized that

flash high-temperature annealing helps to limit the grain boundaries of the out-of-plane substrate, resulting in the device showing a power conversion efficiency of 18.8% compared to 18.0% when using a more standard post-annealing procedure.

2.3.2. Annealing Methods

High-performance perovskite devices need to prepare perovskite films with high crystallinity and good surface morphology [95]. Most current methods for preparing PSCs involve depositing a perovskite precursor solution, adding antisolvent (AS) such as chlorobenzene to induce nucleation, and finally, thermal annealing to vaporize the solvent and promote the crystallization of the perovskite in the desired form [96]. However, this traditional annealing method cannot recover organic solvents, causes much waste, and cannot be applied in large-area preparation. The perovskite layer needs to be annealed at more than 100 °C for 30 min, resulting in a significant increase in manufacturing costs. Hence, people began to work on other low-temperature, rapid annealing methods, such as the solvent vapor annealing method [97], flash infrared annealing method (FIRA) [98], and intense pulsed light annealing [99].

Solvent steam annealing is a common annealing method in perovskite materials. The SVA process involves annealing perovskite films in the presence of polar aprotic solvent vapors (e.g., dimethylformamide, DMF). The introduction of steam in the annealing process is conducive to the long-distance diffusion of precursor ions and molecules. This annealing method has the advantage of promoting the growth of large grain size, reducing grain boundary density, increasing grain size, and forming continuous grains between the anode and cathode contacts of P.V. devices. The annealing process is shown in Figure 15a. Different vapors have different effects on perovskite. Zhao et al. used isopropyl alcohol (IPA) as vapor for annealing and found that it could plasticize the perovskite film and reorganize the structure without causing the film to dewet from the substrate [97]. Zheng et al., using γ -GBL for solvent annealing of $(\text{B.A.})_2(\text{M.A.})_3\text{Pb}_4\text{I}_{13}$, produced a device with an efficiency of less than 5% [100]. Using a solvent with a relatively high solubility of the perovskite precursor (e.g., GBL) allowed for the perovskite film to be completely dewetted from its substrate. Li et al. used chlorobenzene (C.B.) solution steam annealing and found that the surface properties of perovskite can give it better surface contact with PCBM film [101]. Nevertheless, this annealing method also has certain disadvantages. Onkar et al. found that the interaction between cations and polar solvents (such as DMF) with the SVA method resulted in the loss of components, causing changes in the composition of perovskites and reducing their stability [102]. The traditional annealing method requires a long annealing time at a high temperature to crystallize, requires the use of many highly toxic anti-solvents (such as chlorobenzene), and is not conducive to the preparation of large areas. The flash infrared annealing method (FIRA) is a common type of low-temperature annealing method. This kind of preparation method does not require a long time of annealing at high temperatures and does not use anti-solvent. The impact on the environment is minimal, it is capable of rapid nucleation and crystal growth of perovskite from the precursor solution in a few seconds, and the prepared device has relatively high efficiency. There are many other methods with the same principle of flash infrared annealing, which use laser annealing perovskite films. You et al. used a high-energy laser to scan perovskite films at a low substrate temperature. They achieved rapid crystallization within seconds under the irradiation of a high-intensity and high scanning speed laser [103]. Ghahremani et al. were the first to anneal Tri cationic perovskites using xenon lamp millisecond sustained pulses to quickly produce highly efficient PSCs [104]. The microwave annealing process (MAP) is often used to prepare perovskite films, and traditional hot plate annealing usually results in a higher temperature near the substrate than the surface, resulting in uneven nucleation of perovskite. In addition to the above methods, the microwave annealing process (MAP) is often used for the preparation of perovskite films. Traditional hot plate annealing usually causes the temperature near the substrate to be higher than the surface, resulting in uneven nucleation of perovskite. The MAP method can transform microwave radiation

energy inside perovskite to provide a uniform annealing environment for perovskite [105]. Chen et al. used the MAP method to prepare perovskite films and formed micron-sized perovskite crystals, and the device efficiency of the prepared device was as high as 21.59% [105]. Wang et al. modulated the crystallization of perovskite films using the MPT method and found that microwaves can induce high-frequency vibration of dipoles and ions in perovskite and prepare high-quality perovskite films [106]. In addition to the above common annealing methods, researchers have continuously developed a variety of new annealing methods, such as pressure-assisted annealing methods [107], rapid thermal annealing [108], inverted thermal annealing [109], liquid medium annealing [110], and the merged annealing method [63]. Table 2 shows the annealing method for perovskite films and its advantages, and the process is shown in Figure 15. At present, solvent vapor annealing, laser irradiation, and microwave treatment are the three most used methods, each of which has its advantages and scope of application. Solvent vapor annealing can obtain better perovskite films, but long-time high-temperature annealing is needed. The preparation of laser irradiation is fast and can be carried out on a low-temperature substrate. However, the obtained perovskite crystallinity is not very good, and the performance of the battery may be reduced. The microwave treatment method can convert microwave energy into internal energy of perovskite so that perovskite is heated evenly, which is conducive to crystal growth. However, the required temperature is high, and the preparation time is long.

Table 2. The novel annealing method for perovskite films and gain in performances.

Method	Device Structure	Maintained Initial PCE ^a	References
Solvent-vapor annealing	IPA	FTO/c-TiO ₂ /m-TiO ₂ /(BDA)(Cs _{0.1} FA _{0.9}) ₄ Pb ₅ I ₁₆ /dopant-free ST1/Cr/Au.	C:13.9%, M:18.9% [97]
	CB	ITO/PEDOT:PSS/perovskite/PCBM/Al	C:11.86% M:13.40% [101]
	DMSO	ITO/PEDOT:PSS/MAPbI ₃ /PCBM/Ag	C:3.40% M:17.04% [111]
	IPA:DMF = 100:1	ITO/PEDOT:PSS/MAPbI ₃ /PCBM/Ag	C:11.5% M:14.3% [112]
	Water	N\A	N\A [113]
	Hac/CB	ITO/PEDOT:PSS/MAPbI ₃ /PCBM/Ag	C:11.44% M:12.80% [114]
	GBL	ITO/TiO ₂ /MAPbI ₃ /spiro-OMeTAD)/Au	C:13.05% M:16.85% [115]
Laser irradiation		ITO/TiO ₂ /MAPbI ₃ /spiro-OMeTAD)/Au	C:18.3% M:18.1% [98]
	Flash infrared annealing	FTO/TiO ₂ /TiO ₂ -mesoporous/MAPbI ₃ /Spiro/Au	N\A M:19.5% [116]
		FTO/TiO ₂ /perovskite/Spiro/Au	C:19.0% M:19.2% [117]
		FTO/TiO ₂ /CsPb _{1.5} Br _{1.5} /PTAA/Au	N\A M:10.3% [118]
	Laser annealing Intense pulsed light sintering	FTO/TiO ₂ /perovskite/Spiro/Au	C:18.10% M:20.98% [103]
Microwave treatment		FTO/TiO ₂ /perovskite/Spiro/Au	C:8.21% M:11.5% [99]
		ITO/PEDOT:PSS/perovskite/BCP/PCBM/Au	C:11.58% M:13.39% [106]
		ITO/PTAA/perovskite/PCBM/C ₆₀ /BCP/Ag	C:18.33 M:18.59 [105]
Pressure-assisted annealing	FTO/c-TiO ₂ /CsPbBr ₃ /Carbon	C:2.79% M:7.22% [107]	

Table 2. Cont.

Method	Device Structure	Maintained Initial PCE ^a	References
Air-free fast solution	FTO/bl-TiO ₂ /m-TiO ₂ /MAPbI ₃ /Spiro/Au	N\A M:12.10%	[119]
Closed steam annealing method	FTO/TiO ₂ /MAPbI ₃ /Spiro/Au	C:12.35% 13.77%	[120]
Rapid thermal annealing	PET/ITO/PTAA/PFN/PVSK/C60/BCP/Ag	N\A M:14.58%	[108]
Inverted thermal annealing	FTO/c-TiO ₂ /MAPbI ₃ /HTM/Au	C:10.89% M:12.88%	[109]
Liquid medium annealing	ITO/SnO ₂ /FA _{1-x-y} MA _x Cs _y PbI _{3-z} Br _z /SpiroOMeTAD/Au	C:23.15% M:24.04%	[110]
Merged annealing method	ITO/PEDOT:PSS/perovskite/PCBM/Al	C:11.93% M:18.27%	[63]

^a C: efficiency of devices prepared using conventional annealing methods; M: efficiency of devices prepared using novel annealing methods.

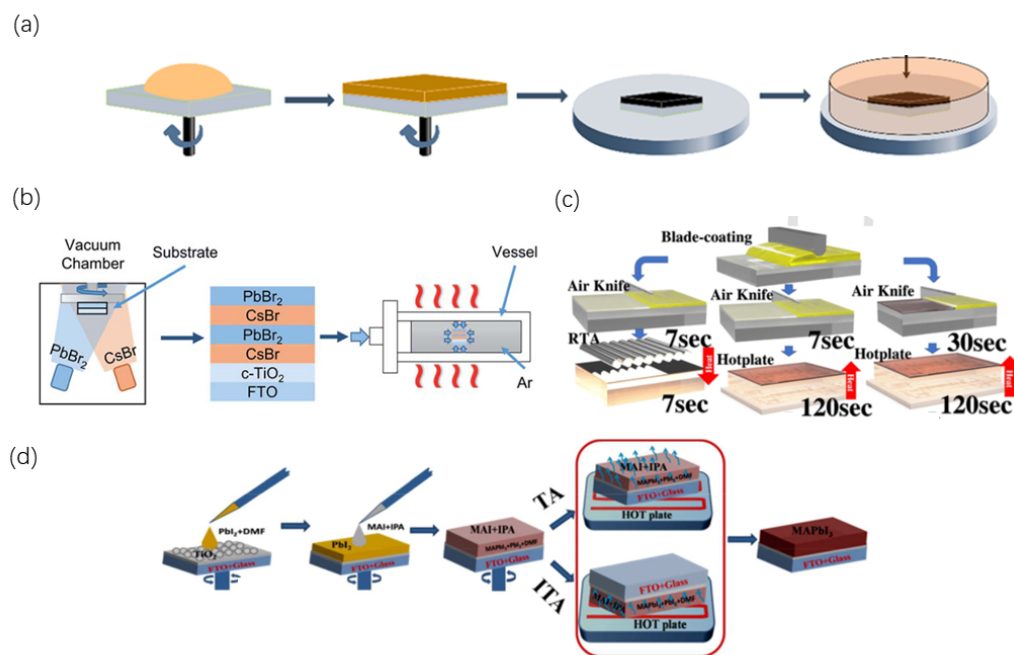


Figure 15. Process of (a) solvent vapor method [97]. Copyright 2021, AMER CHEMICAL SOC publishing. (b) Pressure-assisted annealing process [107]. Copyright 2020, ROYAL SOC CHEMISTRY publishing. (c) Rapid thermal annealing [108]. Copyright 2020, ELSEVIER publishing. (d) Inverted thermal annealing [109]. Copyright 2016, ROYAL SOC CHEMISTRY publishing.

2.3.3. Effect of Temperature on Perovskite under Working Conditions

The performance of the perovskite light absorption layer depends on the electronic structure and other microscopic characteristics, such as band gap carrier effective mass, among which the band gap size is closely related to its light absorption capacity. In addition to the intrinsic structural factors, temperature is one of the critical external factors affecting the material band gap: experiments have found that perovskite materials change band gap at different temperatures, and the band gap of perovskite materials increases with the increase in temperature, which has a significant impact on the photoelectric properties. Studies have shown that the change in material band gap with temperature is mainly caused by two aspects: lattice thermal expansion and lattice thermal vibration.

Adrián et al. investigated the relationship between temperature and bandgap of perovskite [121]. The change in P.L. spectra and temperature in the stability range of the tetragonal phase of MAPbI₃ is shown in Figure 16a. With the decrease in temperature, the main P.L. peak showed a gradual redshift and sharpening. Figure 16b plots the values of fitting parameters corresponding to P.L. peak maximum energy E_0 as a function of temperature. Although we cannot tell the absolute values of bandgap and/or exciton binding energy from the line shape fits, although we cannot judge the exciton binding energy and absolute value of band gap from linear fitting, the shift in P.L. peak energy E_0 with temperature largely depends on the shift in gap. For MAPbI₃, the gap decreases linearly with the decrease in temperature.

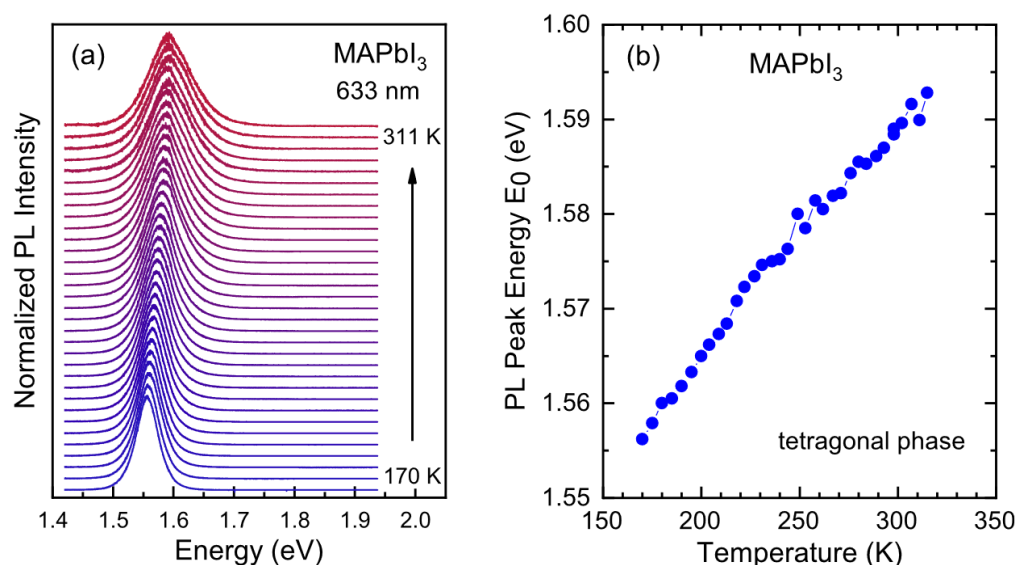


Figure 16. (a) P.L. spectra of MAPbI₃ measured at different temperatures in the range of stability of the tetragonal phase (ca. 170 to 311 K) using the red line (633 nm) for excitation. The spectra were normalized to their maximum intensity and plotted with a vertical shift for increasing temperature. Change in color indicates an increase in temperature. (b) A plot of the temperature dependence of the maximum peak position E_0 of the spectra displayed in part (a) [121]. Copyright 2019, AMER CHEMICAL SOC publishing.

Aydin et al. demonstrated temperature-dependent J–V measurements in a laboratory environment [122] by varying the temperature between 25 and 75 °C in a simulated AM1.5G spectrum over the expected operating temperature range (Figure 17a). In the study, we can find that with the increased temperature, the J_{SC} of the device decreases. This current mismatch is because the E_g of c-Si and perovskite layers varies with temperature: c-Si E_g narrows with increasing temperature, while perovskite E_g broadens.

The temperature-dependent EQE in series (Figure 17b) further elucidates E_g displacement as a function of temperature. We can see from Figure 17c that the J_{SC} , EQE (obtained by spectral integration of the product of EQE and the incident solar spectrum) of the bottom cell of c-Si increase with temperature due to the additional contribution of longer wavelength photons (c-Si E_g redshift) and shorter wavelength photons (perovskite E_g blue shift). More light from two different spectral ranges is coupled in the c-Si bottom cell.

Temperature also will make the perovskite degrade. MA⁺ and I[−] ions with lower activation energy may migrate in high temperatures [123]. Smaller perovskite crystals are more likely to decompose than bulk perovskite crystals due to higher defect distribution density and more ion migration channels provided by the surface and grain boundaries, thus further reducing the activation energy [124]. Chen et al. used TGA-FTIR to study the thermal decomposition process of mixed cationic perovskite FA_xMA_{1-x}PbI₃ under different F.A. and M.A. cation ratios. The experimental results show that the thermal decomposition of M.A. and F.A. cations occurs in all stages of the decomposition process of mixed cation

perovskite. Chen et al. used TGA-FTIR to study the thermal decomposition process of mixed cationic perovskite $\text{FA}_x\text{MA}_{1-x}\text{PbI}_3$ under different FA^+ and MA^+ cation ratios. The experimental results show that the thermal decomposition of M.A. and F.A. cations occurs in all stages of the decomposition process of mixed cation perovskite. Figure 18 shows the temperature at which the perovskite begins to decompose at different proportions.

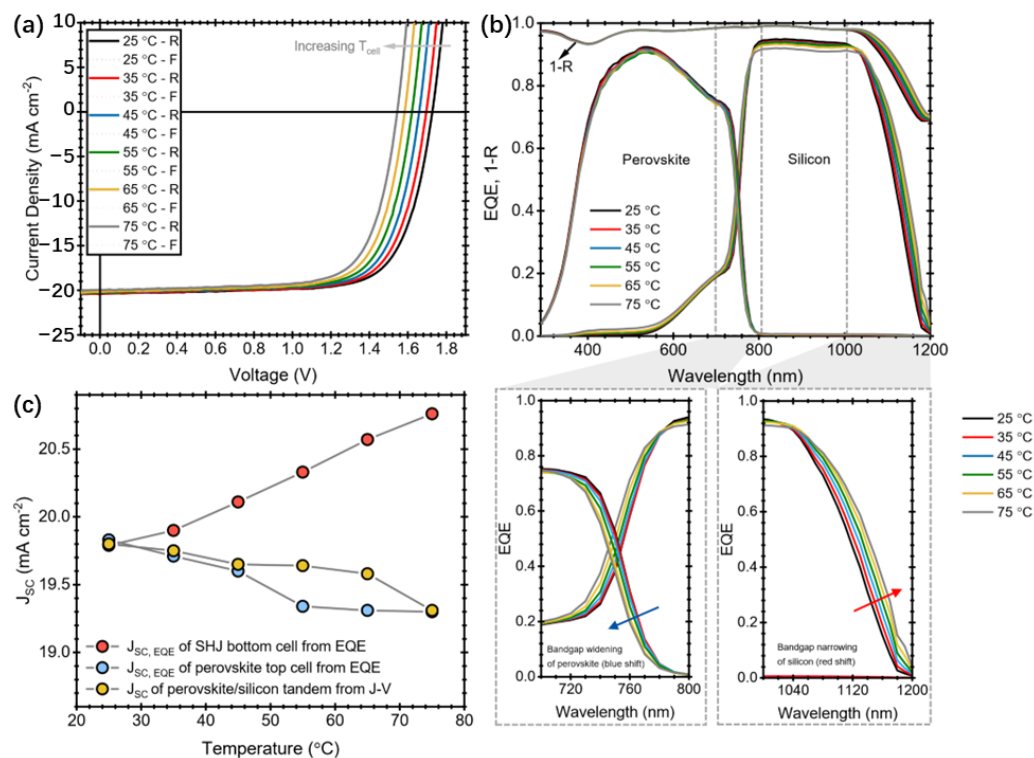


Figure 17. Temperature-dependent J–V (R: reverse scan; F: forwards scan) (a) and EQE and 1–R (R is reflectance) characteristics. (b) of perovskite/silicon tandem devices. The bottom of b shows a magnification into the region of the band edge for both sub-cells. (c) Temperature-dependent change in EQE measured current density (J_{SC} , EQE) values for both sub-cells and the J–V measured current density (J_{SC}) of a tandem solar cell, showing current limiting conditions. The arrow on the right figure shows the change direction of EQE with increasing temperature. [122] Copyright 2019, ELSEVIER publishing.

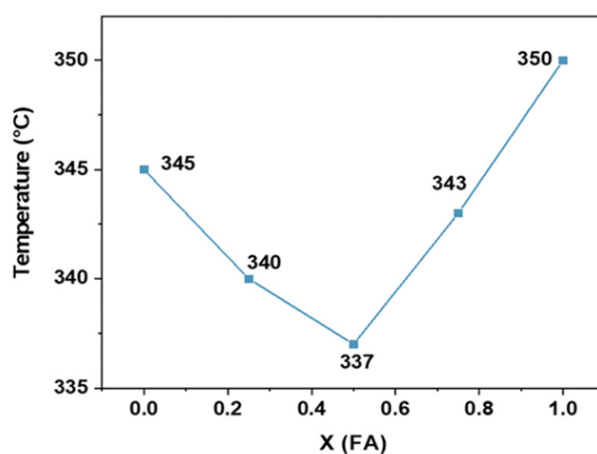


Figure 18. The variation in decomposition temperature of perovskite with x values [125]. Copyright 2023, WILEY-VCH VERLAG GMBH publishing.

PSCs have many degradation factors, and researchers are focused on finding ways to improve their stability. Sputtered transparent conductive oxides (TCOs) such as indium tin oxide (ITO) [126,127], zinc-doped tin oxide (ZTO) [126], or aluminum-doped zinc oxide (AZO) [128] as top contacts can effectively improve the stability of the device, which can effectively prevent the leakage of volatile organic materials and prevent the migration of ions and metal atoms. However, the sputtering method may damage the charge transport layer and the underlying perovskite layer, thus limiting the performance of the device. Annealing can effectively reduce the device efficiency loss caused by sputtering damage. Mariotti et al. prepared a perovskite/silicon tandem solar cell, sputtered ITO as the top electrode, and found that sputtering would damage the performance of the device. The device was annealed at different temperatures, and the device had the best performance at 300 °C [129]. Luo [130] and Liu et al. [131], when preparing perovskite/silicon-laminated solar cells, both annealed at 200 °C for 10 min to recover sputtering damage before preparing perovskite top cells.

3. Temperature Coefficient of Perovskite Cells in Operation

The temperature of the working environment has a strong influence on the stability and performance of the perovskite layer. For example, the band gap, surface tension, charge diffusion, and recombination process will adjust with the temperature change [132]. A positive temperature coefficient (T.C.) value means the performance increases with increasing temperature, while a negative T.C. value means the performance decreases with increasing temperature [133]. a-Si, CdTe, and cupric indium gallium selenide (CIGS) are negative T.C. values for thin film solar cells [134]. The T.C. of PSCs is between 0.18%/K [128] and 0.33%/K [135], and several studies also show nonlinear T.C.

Methylammonium lead iodide ($\text{CH}_3\text{NH}_3\text{PbI}_3$, MAPbI₃) perovskite exhibits two phase transitions, one occurring under actual working conditions (310 K). Compared with MAPbI₃, triatomic perovskite exhibits this phase transition at temperatures higher than 420 K [136]. Research has revealed that carrier transport does not limit device performance at medium to high temperatures [137]. However, ion migration also influences transport properties, which has been shown to be related to the temperature [138]. The optical properties of perovskite are essential for optimizing the design of optoelectronic devices and are analyzed to be relevant to the temperature [122]. Unlike most semiconductors, the band gap of perovskite increases with the rising temperature. In addition, the degradation often appears in the interface of the perovskite layer with the hole transport layer or ETL. Many studies have shown that changes in the interface properties and the mobility of the selective contact transport layer alter the performance of PSCs [132]. PSCs are constituted of many different organic and inorganic layers. The T.C. of a PSC is not only dependence on the perovskite layer but also dependence on each layer and each interface.

Marko et al. used Solar Cell Capacitance Simulator (SCAPS-1D) software to investigate the effect of temperature on lead-free tin-based PSCs' electrical and photovoltaic parameters. They calculated the T.C.s of these parameters [139]. The dark current–voltage analysis shows that the barrier height T.C. is positive, and the ideal factor T.C. is negative. The light J–V curves show that all photovoltaic parameters are negative T.C.s. The absolute T.C. of J_{sc} , V_{oc} , FF , and PCE is 9 mA/cm^2 per K, 1.6 mV per K, 0.031 per K, and 0.074 per K, as Figure 19 shows. There are few studies on the effect of temperature on CPSC performance changes, which is of great significance for understanding the effect of temperature on CPSC design. Bhandari et al. studied the T.C. of carbon-based devices [140] having MAPbCl [MAPbI_{3-x}Cl_x] and CsFAMA [Cs_{0.05}(FA_{0.83}MA_{0.17})_{0.95}Pb(I_{0.83}Br_{0.17})₃]. MAPbCl-based CPSCs maintained a power conversion efficiency (PCE) of approximately 9% to 11.7% when dealing with individual devices in the range of 5–65 °C.

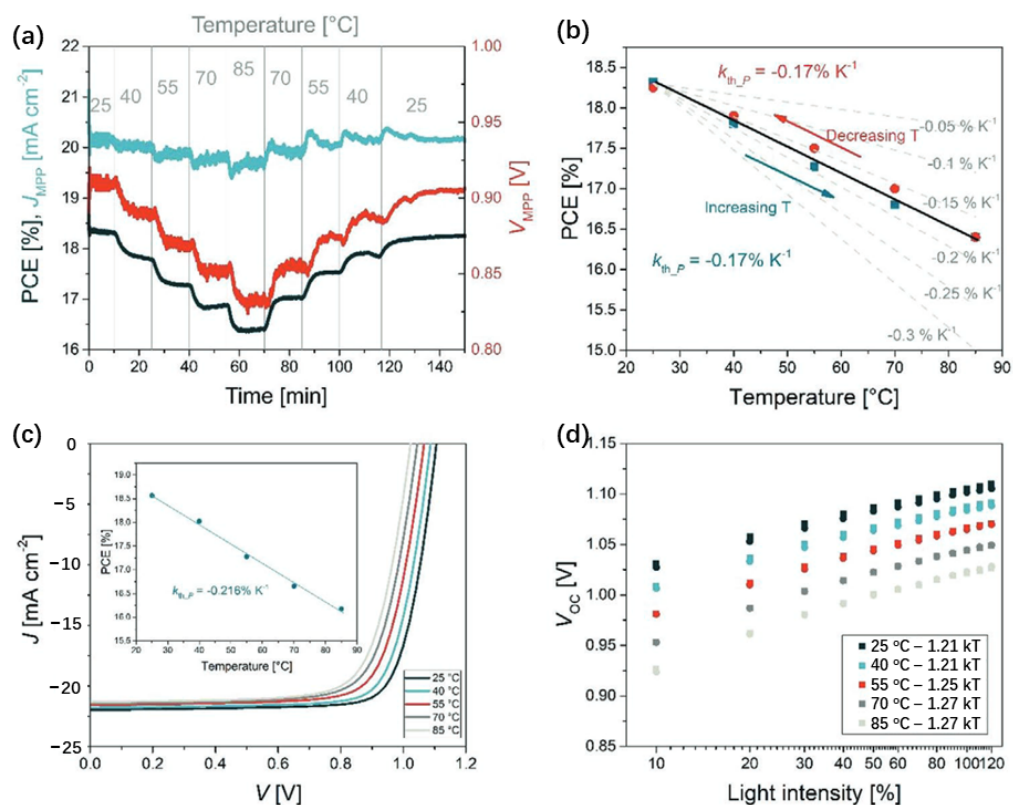


Figure 19. (a) MPP track of the fabricated perovskite single-junction device by changing the temperature between 25 and 85 °C with a 15 °C step. J_{MPP} (blue) and V_{MPP} (red) are also plotted. (b) PCE in dependence on temperature. The linear fit shows the temperature coefficients: the solid line shows the measured one, while the dashed lines indicate how other power temperature coefficient values would manifest. Arrows indicate the direction in which the test temperature increases and decreases. (c) J–V characteristics at 100 mW cm^{-2} intensity. (d) V_{oc} dependence on light intensity and temperature for the tested perovskite device [38]. Copyright 2020, WILEY-VCH VERLAG GMBH publishing.

In contrast, dual mesoscopic devices based on CsFAMA show a PCE variation of about 14 to 16% under the same temperature window. The average T.C. values of MAPICl and CsFAMA are on the order of 10^{-4} , which means that the performance of these devices holds up better despite the thermal stress. For PSCs, the effect of temperature on their optical properties is relatively small.

4. ISOS Standard and Influence of Operating Temperature

With the development of perovskite devices, testing the performance of solar cells is inevitable. Different test conditions will affect the stability results, and the properties of different materials are different. They cannot be tested using silicon cell standards, so many studies lack consistency in experimental testing, which is not conducive to data comparison, and it is impossible to determine the various degradation factors and failure mechanisms. Therefore, there is a need to develop test standards to better help us understand the degradation pattern of solar cells. Mark et al. customized a set of test standards for perovskite cells by drawing on the International Summit on Organic Photovoltaic Stability (ISOS) protocol developed in the OPV field [141].

According to the different reasons for the decomposition of perovskite materials, the researchers have set seven test standards. Each set has three levels: the larger the number, the higher the test level, and the more reliable the data.

- (1) ISOS-D (dark storage studies): The purpose of this test is to provide information on the stability of the solar cell against oxygen, moisture, and other atmospheric components present in the air (such as CO₂, NO_x, and H₂S) and high temperatures. The test is performed in the absence of a light source, without load. Level 1 is room temperature, ambient humidity; Level 2 is 65 or 85 °C with ambient humidity; Level 3 is 65 or 85 °C with 85% relative humidity.
- (2) ISOS-V: Electrical bias can cause the degradation of PSCs by controlling the interaction of ions and charges, so electrical bias can also affect the stability of PSCs. Test conditions are as follows: no light source, such as applying positive bias, the bias value can be set to V_{MPP} , V_{oc} , E_g/q , J_{sc} . If negative bias is applied, the bias value can be set to $-V_{oc}$, $-J_{MPP}$. The difference in levels 1, 2, and 3 for this test is the same as ISOS-D. The negative bias is mainly applied to simulate the shadow effect during the operation of the module. V_{oc} represents the partially blocked module with an external bypass diode, and J_{MPP} represents the partially blocked module without an external bypass diode.
- (3) ISOS-L (light stability): The light source is recommended to be a sunlight simulator without conditions. It can also be replaced by LED lights or halogen lamps, but to indicate the nature of the light source (will be described in detail in the next part). Level 1 is room temperature, ambient humidity, and load is MPP point voltage or open voltage; Level 2 is 65 or 85 °C, ambient humidity, and the load is MPP point voltage or open voltage; Level 3 is 65 or 85 °C, 50% relative humidity, and the load is MPP point voltage.
- (4) ISOS-O (outdoor stability): The light source is sunlight, and the geographical location should be indicated. All levels are outdoor temperature humidity. The difference is that the level 1 load is MPP point voltage or open voltage, the test light source for device performance is sunlight simulator; the Level 2 load is MPP point voltage or open voltage, and the device performance test light source is sunlight; Level 3 load is MPP point voltage, device performance test light source is sunlight simulator and sunlight.
- (5) ISOS-T (temperature cycle stability): No light source, no load. Levels 1 and 2 are from room temperature to 65 or 85 °C, ambient humidity; Level 3 is from -40 to 85 °C, with relative humidity of less than 55%.
- (6) ISOS-LC (photocycle stability): Since the degradation of PSCs under dark conditions has certain reversibility, the diurnal cycle is simulated by adjusting the light and dark of the light source, the diurnal cycle is simulated by adjusting the light and dark of the light source. Level 1 is room temperature, ambient humidity, and load is MPP point voltage or open voltage; Level 2 is 65 or 85 °C, ambient humidity, and the load is MPP point voltage or open voltage; Level 3 is 65 or 85 °C, less than 50% relative humidity, and the load is MPP point voltage.
- (7) ISOS-LT (light temperature cycle stability): The light source is recommended to be a sunlight simulator, which LED lights or halogen lamps can also replace without conditions, and the load is MPP point voltage or open voltage. Level 1 is from room temperature to 65 °C, ambient humidity; Level 2 is from 5 to 65 degrees Celsius, 50% relative humidity; Level 3 is from -25 to 65 °C with 50% relative humidity.

5. Summary and Outlook

In summary, we accurately captured the critical points discussed regarding the influence of temperature on various layers of PSCs and their overall performance. We have broken down the key elements as follows:

- Influence of Temperature on Different Layers: ETL, HTL, and perovskite layer: The temperature during manufacturing significantly affects the surface morphology of the device and has implications for electrical performance and service life. Higher annealing temperatures, for example, can improve film quality, grain size, and overall compactness, enhancing the efficiency of the cells.

- Effect of External Temperature: Limited impact on cell performance: Interestingly, the change in external temperature (presumably during actual operational conditions) has been observed to have little influence on the performance of the cells. This suggests a certain level of robustness or insulation against external temperature variations.
- Need for Improved Annealing Manufacturing Methods: Optimizing annealing processes: Given the significant impact of manufacturing temperature on device characteristics, there is a call to develop more appropriate annealing methods. This optimization is crucial for improving not only the performance but also the stability of photovoltaic devices.
- Broad Application Prospects for PSCs: Positive outlook: Despite the challenges and considerations related to temperature, the overall outlook for perovskite solar cells is optimistic. The expectation is that, with advancements in manufacturing processes and annealing methods, PSCs will have a broad application prospect. This suggests a promising future for perovskite-based photovoltaic technology.

In conclusion, our summary provides a clear understanding of the importance of temperature in the fabrication and performance of perovskite solar cells, emphasizing the need for careful optimization of annealing processes to unlock the full potential of these solar devices.

Author Contributions: Conceptualization, S.W. and P.G.; methodology, S.W. and C.L.; software, S.W.; validation, S.W., C.L., S.Y.L. and P.G.; formal analysis, S.W.; investigation, S.W.; resources, P.G.; data curation, S.W.; writing—original draft preparation, S.W.; writing—review and editing, P.G. and S.Y.L.; visualization, S.W.; supervision, P.G.; project administration, P.G.; funding acquisition, P.G. All authors have read and agreed to the published version of the manuscript.

Funding: This work was supported by the National Natural Science Foundation of China (Grant No. 22175180, 52311530673).

Conflicts of Interest: The authors declare no conflicts of interest.

References

1. Gao, P.; Grätzel, M.; Nazeeruddin, M.K. Organohalide Lead Perovskites for Photovoltaic Applications. *Environ. Sci.* **2014**, *7*, 2448–2463. [[CrossRef](#)]
2. Mohd Yusoff, A.R.B.; Gao, P.; Nazeeruddin, M.K. Recent progress in organohalide lead perovskites for photovoltaic and optoelectronic applications. *Coord. Chem. Rev.* **2018**, *373*, 258–294. [[CrossRef](#)]
3. Blancon, J.-C.; Stier, A.V.; Tsai, H.; Nie, W.; Stoumpos, C.C.; Traoré, B.; Pedesseau, L.; Kepenekian, M.; Katsutani, F.; Noe, G.T.; et al. Scaling law for excitons in 2D perovskite quantum wells. *Nat. Commun.* **2018**, *9*, 2254. [[CrossRef](#)] [[PubMed](#)]
4. Hu, L.; Zhao, Q.; Huang, S.; Zheng, J.; Guan, X.; Patterson, R.; Kim, J.; Shi, L.; Lin, C.-H.; Lei, Q.; et al. Flexible and efficient perovskite quantum dot solar cells via hybrid interfacial architecture. *Nat. Commun.* **2021**, *12*, 466. [[CrossRef](#)] [[PubMed](#)]
5. Sun, X.; Deng, X.; Li, Z.; Xiong, B.; Zhong, C.; Zhu, Z.; Li, Z.; Jen, A.K. -Y. Dopant-Free Crossconjugated Hole-Transporting Polymers for Highly Efficient Perovskite Solar Cells. *Adv. Sci.* **2020**, *7*, 1903331. [[CrossRef](#)] [[PubMed](#)]
6. Bella, F.; Griffini, G.; Correa-Baena, J.-P.; Saracco, G.; Grätzel, M.; Hagfeldt, A.; Turri, S.; Gerbaldi, C. Improving efficiency and stability of perovskite solar cells with photocurable fluoropolymers. *Science* **2016**, *354*, 203–206. [[CrossRef](#)]
7. Zhang, J.; Sun, Q.; Chen, Q.; Wang, Y.; Zhou, Y.; Song, B.; Yuan, N.; Ding, J.; Li, Y. High Efficiency Planar p-i-n Perovskite Solar Cells Using Low-Cost Fluorene-Based Hole Transporting Material. *Adv. Funct. Mater.* **2019**, *29*, 1900484. [[CrossRef](#)]
8. Yu, X.; Zou, X.; Cheng, J.; Chen, D.; Yao, Y.; Chang, C.; Liu, B.; Wang, J.; Zhou, Z.; Li, G. Investigation on Low-temperature Annealing Process of Solution-processed TiO₂ Electron Transport Layer for Flexible Perovskite Solar Cell. *Materials* **2020**, *13*, 1031. [[CrossRef](#)] [[PubMed](#)]
9. Dualeh, A.; Gao, P.; Seok, S.I.; Nazeeruddin, M.K.; Grätzel, M. Thermal Behavior of Methylammonium Lead-Trihalide Perovskite Photovoltaic Light Harvesters. *Chem. Mater.* **2014**, *26*, 6160–6164. [[CrossRef](#)]
10. Liu, X.; Wu, J.; Li, G.; Guo, Q.; Song, Z.; Yang, Y.; Wang, X.; Lan, Z.; Lin, J. Defect Control Strategy by Bifunctional Thioacetamide at Low Temperature for Highly Efficient Planar Perovskite Solar Cells. *ACS Appl. Mater. Interfaces* **2020**, *12*, 12883–12891. [[CrossRef](#)] [[PubMed](#)]
11. Wu, W.-Q.; Chen, D.; Cheng, Y.-B.; Caruso, R.A. Low-Temperature Solution-Processed Amorphous Titania Nanowire Thin Films for 1 cm² Perovskite Solar Cells. *ACS Appl. Mater. Interfaces* **2020**, *12*, 11450–11458. [[CrossRef](#)]
12. Liu, M.; Johnston, M.B.; Snaith, H.J. Efficient planar heterojunction perovskite solar cells by vapour deposition. *Nature* **2013**, *501*, 395–398. [[CrossRef](#)] [[PubMed](#)]

13. Tan, H.; Jain, A.; Voznyy, O.; Lan, X.; García De Arquer, F.P.; Fan, J.Z.; Quintero-Bermudez, R.; Yuan, M.; Zhang, B.; Zhao, Y.; et al. Efficient and stable solution-processed planar perovskite solar cells via contact passivation. *Science* **2017**, *355*, 722–726. [[CrossRef](#)] [[PubMed](#)]
14. Burschka, J.; Pellet, N.; Moon, S.-J.; Humphry-Baker, R.; Gao, P.; Nazeeruddin, M.K.; Grätzel, M. Sequential deposition as a route to high-performance perovskite-sensitized solar cells. *Nature* **2013**, *499*, 316–319. [[CrossRef](#)]
15. Lu, H.; Zhong, J.; Ji, C.; Zhao, J.; Li, D.; Zhao, R.; Jiang, Y.; Fang, S.; Liang, T.; Li, H.; et al. Fabricating an optimal rutile TiO₂ electron transport layer by delicately tuning TiCl₄ precursor solution for high performance perovskite solar cells. *Nano Energy* **2020**, *68*, 104336. [[CrossRef](#)]
16. Hu, H.; Dong, B.; Hu, H.; Chen, F.; Kong, M.; Zhang, Q.; Luo, T.; Zhao, L.; Guo, Z.; Li, J.; et al. Atomic Layer Deposition of TiO₂ for a High-Efficiency Hole-Blocking Layer in Hole-Conductor-Free Perovskite Solar Cells Processed in Ambient Air. *ACS Appl. Mater. Interfaces* **2016**, *8*, 17999–18007. [[CrossRef](#)] [[PubMed](#)]
17. Song, S.; Kang, G.; Pyeon, L.; Lim, C.; Lee, G.-Y.; Park, T.; Choi, J. Systematically Optimized Bilayered Electron Transport Layer for Highly Efficient Planar Perovskite Solar Cells ($\eta = 21.1\%$). *ACS Energy Lett.* **2017**, *2*, 2667–2673. [[CrossRef](#)]
18. Basavaraj, K.; Nyayban, A.; Panda, S. Structural phase transitions and elastic properties of TiO₂ polymorphs: Ab-initio study. *IOP Conf. Ser. Mater. Sci. Eng.* **2022**, *1248*, 012064. [[CrossRef](#)]
19. Reyes-Coronado, D.; Rodriguez-Gattorno, G.; Espinosa-Pesqueira, M.E.; Cab, C.; De Coss, R.; Oskam, G. Phase-pure TiO₂ nanoparticles: Anatase, brookite and rutile. *Nanotechnology* **2008**, *19*, 145605. [[CrossRef](#)] [[PubMed](#)]
20. Shannon, R.D.; Pask, J.A. Kinetics of the Anatase-Rutile Transformation. *J. Am. Ceram. Soc.* **1965**, *48*, 391–398. [[CrossRef](#)]
21. Varghese, O.K.; Gong, D.; Paulose, M.; Grimes, C.A.; Dickey, E.C. Crystallization and high-temperature structural stability of titanium oxide nanotube arrays. *J. Mater. Res.* **2003**, *18*, 156–165. [[CrossRef](#)]
22. Rambabu, Y.; Jaiswal, M.; Roy, S.C. Effect of annealing temperature on the phase transition, structural stability and photo-electrochemical performance of TiO₂ multi-leg nanotubes. *Catal. Today* **2016**, *278*, 255–261. [[CrossRef](#)]
23. Ma, J.-S.; Wen, M.-C.; Lu, C.-H. Reaction mechanism and kinetics analysis of the phase transformation of TiO₂ from the anatase phase to the rutile phase. *J. Mater. Sci. Mater. Electron.* **2013**, *24*, 2506–2512. [[CrossRef](#)]
24. Lin, L.; Jones, T.W.; Yang, T.C.; Duffy, N.W.; Li, J.; Zhao, L.; Chi, B.; Wang, X.; Wilson, G.J. Inorganic Electron Transport Materials in Perovskite Solar Cells. *Adv. Funct. Mater.* **2021**, *31*, 2008300. [[CrossRef](#)]
25. Hu, X.; Liu, C.; Zhang, Z.; Jiang, X.; Garcia, J.; Sheehan, C.; Shui, L.; Priya, S.; Zhou, G.; Zhang, S.; et al. 22% Efficiency Inverted Perovskite Photovoltaic Cell Using Cation-Doped Brookite TiO₂ Top Buffer. *Adv. Sci.* **2020**, *7*, 2001285. [[CrossRef](#)] [[PubMed](#)]
26. Kogo, A.; Sanehira, Y.; Ikegami, M.; Miyasaka, T. Brookite TiO₂ as a low-temperature solution-processed mesoporous layer for hybrid perovskite solar cells. *J. Mater. Chem. A* **2015**, *3*, 20952–20957. [[CrossRef](#)]
27. Wang, Y.; Wan, J.; Ding, J.; Hu, J.; Wang, D. A Rutile TiO₂ Electron Transport Layer for the Enhancement of Charge Collection for Efficient Perovskite Solar Cells. *Angew. Chem. Int. Ed.* **2019**, *58*, 9414–9418. [[CrossRef](#)] [[PubMed](#)]
28. Shahvaranfard, F.; Altomare, M.; Hou, Y.; Hejazi, S.; Meng, W.; Osuagwu, B.; Li, N.; Brabec, C.J.; Schmuki, P. Engineering of the Electron Transport Layer/Perovskite Interface in Solar Cells Designed on TiO₂ Rutile Nanorods. *Adv. Funct. Mater.* **2020**, *30*, 1909738. [[CrossRef](#)]
29. Malevu, T.D.; Mwankemwa, B.S.; Motloung, S.V.; Tshabalala, K.G.; Ocaya, R.O. Effect of annealing temperature on nano-crystalline TiO₂ for solar cell applications. *Phys. E Low-Dimens. Syst. Nanostruct.* **2019**, *106*, 127–132. [[CrossRef](#)]
30. Hossain, M.F. Annealing effect of E-beam evaporated TiO₂ films and their performance in perovskite solar cells. *J. Photochem.* **2018**, *360*, 109–116. [[CrossRef](#)]
31. Lv, Y.; Yuan, R.; Cai, B.; Bahrami, B.; Chowdhury, A.H.; Yang, C.; Wu, Y.; Qiao, Q.; Liu, S.; Zhang, W. High-Efficiency Perovskite Solar Cells Enabled by Anatase TiO₂ Nanopyramid Arrays with an Oriented Electric Field. *Angew. Chem.* **2020**, *132*, 12067–12074. [[CrossRef](#)]
32. Kim, B.J.; Kim, D.H.; Lee, Y.-Y.; Shin, H.-W.; Han, G.S.; Hong, J.S.; Mahmood, K.; Ahn, T.K.; Joo, Y.-C.; Hong, K.S.; et al. Highly efficient and bending durable perovskite solar cells: Toward a wearable power source. *Energy Environ. Sci.* **2015**, *8*, 916–921. [[CrossRef](#)]
33. Hsu, C.-H.; Chen, K.-T.; Lin, L.-Y.; Wu, W.-Y.; Liang, L.-S.; Gao, P.; Qiu, Y.; Zhang, X.-Y.; Huang, P.-H.; Lien, S.-Y.; et al. Tantalum-Doped TiO₂ Prepared by Atomic Layer Deposition and Its Application in Perovskite Solar Cells. *Nanomaterials* **2021**, *11*, 1504. [[CrossRef](#)] [[PubMed](#)]
34. Manabeng, M.; Mwankemwa, B.S.; Ocaya, R.O.; Motaung, T.E.; Malevu, T.D. A Review of the Impact of Zinc Oxide Nanostructure Morphology on Perovskite Solar Cell Performance. *Processes* **2022**, *10*, 1803. [[CrossRef](#)]
35. Fakharuddin, A.; Di Giacomo, F.; Ahmed, I.; Wali, Q.; Brown, T.M.; Jose, R. Role of morphology and crystallinity of nanorod and planar electron transport layers on the performance and long term durability of perovskite solar cells. *J. Power Sources* **2015**, *283*, 61–67. [[CrossRef](#)]
36. Tang, J.-F.; Tseng, Z.-L.; Chen, L.-C.; Chu, S.-Y. ZnO nanowalls grown at low-temperature for electron collection in high-efficiency perovskite solar cells. *Sol. Energy Mater. Sol. Cells* **2016**, *154*, 18–22. [[CrossRef](#)]
37. Leonardi, S. Two-Dimensional Zinc Oxide Nanostructures for Gas Sensor Applications. *Chemosensors* **2017**, *5*, 17. [[CrossRef](#)]
38. Li, Y.-F. First-Principles Prediction of the ZnO Morphology in the Perovskite Solar Cell. *J. Phys. Chem. C* **2019**, *123*, 14164–14172. [[CrossRef](#)]

39. Cao, H.L.; Qian, X.F.; Gong, Q.; Du, W.M.; Ma, X.D.; Zhu, Z.K. Shape- and size-controlled synthesis of nanometre ZnO from a simple solution route at room temperature. *Nanotechnology* **2006**, *17*, 3632–3636. [CrossRef]
40. Pan, Z.W.; Dai, Z.R.; Wang, Z.L. Nanobelts of Semiconducting Oxides. *Science* **2001**, *291*, 1947–1949. [CrossRef]
41. Adnan, M.; Usman, M.; Ali, S.; Javed, S.; Islam, M.; Akram, M.A. Aluminum Doping Effects on Interface Depletion Width of Low Temperature Processed ZnO Electron Transport Layer-Based Perovskite Solar Cells. *Front. Chem.* **2022**, *9*, 795291. [CrossRef]
42. Niu, H.; Fang, C.; Wei, X.; Wang, H.; Wan, L.; Li, Y.; Mao, X.; Xu, J.; Zhou, R. Magnetron sputtered ZnO electron transporting layers for high performance perovskite solar cells. *Dalton Trans.* **2021**, *50*, 6477–6487. [CrossRef] [PubMed]
43. Yun, S.; Guo, T.; Li, Y.; Gao, X.; Huang, A.; Kang, L. Well-ordered vertically aligned ZnO nanorods arrays for high-performance perovskite solar cells. *Mater. Res. Bull.* **2020**, *130*, 110935. [CrossRef]
44. Al Jarrah, R.M.; Kadhem, E.M.; Alkhayatt, A.H.O. Annealing and operating temperatures effect on spray-deposited nanocrystalline ZnO thin-film gas sensor. *Appl. Phys. A* **2022**, *128*, 527. [CrossRef]
45. Khambunkoed, N.; Homnan, S.; Gardchareon, A.; Chattrapiban, N.; Songsiriritthigul, P.; Wongratanaphisan, D.; Ruankham, P. Fully-covered slot-die-coated ZnO thin films for reproducible carbon-based perovskite solar cells. *Mater. Sci. Semicond. Process.* **2021**, *136*, 106151. [CrossRef]
46. Zhou, Y.; Li, X.; Lin, H. To Be Higher and Stronger—Metal Oxide Electron Transport Materials for Perovskite Solar Cells. *Small* **2020**, *16*, 1902579. [CrossRef] [PubMed]
47. Dong, Q.; Shi, Y.; Wang, K.; Li, Y.; Wang, S.; Zhang, H.; Xing, Y.; Du, Y.; Bai, X.; Ma, T. Insight into Perovskite Solar Cells Based on SnO₂ Compact Electron-Selective Layer. *J. Phys. Chem. C* **2015**, *119*, 10212–10217. [CrossRef]
48. Xiong, L.; Guo, Y.; Wen, J.; Liu, H.; Yang, G.; Qin, P.; Fang, G. Review on the Application of SnO₂ in Perovskite Solar Cells. *Adv. Funct. Mater.* **2018**, *28*, 1802757. [CrossRef]
49. Ke, W.; Zhao, D.; Cimaroli, A.J.; Grice, C.R.; Qin, P.; Liu, Q.; Xiong, L.; Yan, Y.; Fang, G. Effects of annealing temperature of tin oxide electron selective layers on the performance of perovskite solar cells. *J. Mater. Chem. A* **2015**, *3*, 24163–24168. [CrossRef]
50. Wang, Y.; Gao, P.; Fan, X.; Li, J.; Guo, P.; Huang, L.; Sun, J. Effect of SnO₂ Annealing Temperature on the Performance of Perovskite Solar Cells. *J. Inorg. Mater.* **2021**, *36*, 168. [CrossRef]
51. Progress and Challenges of SnO₂ Electron Transport Layer for Perovskite Solar Cells: A Critical Review. Available online: <https://onlinelibrary.wiley.com/doi/epdf/10.1002/solr.202100983> (accessed on 24 July 2023).
52. Wang, Q.; Peng, C.; Du, L.; Li, H.; Zhang, W.; Xie, J.; Qi, H.; Li, Y.; Tian, L.; Huang, Y. Enhanced Performance of Perovskite Solar Cells via Low-Temperature-Processed Mesoporous SnO₂. *Adv. Mater. Int.* **2020**, *7*, 1901866. [CrossRef]
53. Jia, J.; Dong, J.; Wu, J.; Wei, H.; Cao, B. Combustion procedure deposited SnO₂ electron transport layers for high efficient perovskite solar cells. *J. Alloys Compd.* **2020**, *844*, 156032. [CrossRef]
54. Liu, J.; Li, N.; Dong, Q.; Li, J.; Qin, C.; Wang, L. Tailoring electrical property of the low-temperature processed SnO₂ for high-performance perovskite solar cells. *Sci. China Mater.* **2019**, *62*, 173–180. [CrossRef]
55. Sun, Y.; Zhang, J.; Yu, H. Room-temperature electrochemically deposited polycrystalline SnO₂ with adjustable work function for high-efficiency perovskite solar cells. *J. Mater. Chem. A* **2023**, *11*, 901–913. [CrossRef]
56. Xu, J.; Buin, A.; Ip, A.H.; Li, W.; Voznyy, O.; Comin, R.; Yuan, M.; Jeon, S.; Ning, Z.; McDowell, J.J.; et al. Perovskite–fullerene hybrid materials suppress hysteresis in planar diodes. *Nat. Commun.* **2015**, *6*, 7081. [CrossRef] [PubMed]
57. Jeng, J.; Chiang, Y.; Lee, M.; Peng, S.; Guo, T.; Chen, P.; Wen, T. CH₃NH₃PbI₃ Perovskite/Fullerene Planar-Heterojunction Hybrid Solar Cells. *Adv. Mater.* **2013**, *25*, 3727–3732. [CrossRef]
58. Sun, S.; Salim, T.; Mathews, N.; Duchamp, M.; Boothroyd, C.; Xing, G.; Sum, T.C.; Lam, Y.M. The origin of high efficiency in low-temperature solution-processable bilayer organometal halide hybrid solar cells. *Energy Environ. Sci.* **2014**, *7*, 399–407. [CrossRef]
59. Niu, G.; Wang, S.; Li, J.; Li, W.; Wang, L. Oxygen doping in nickel oxide for highly efficient planar perovskite solar cells. *J. Mater. Chem. A* **2018**, *6*, 4721–4728. [CrossRef]
60. Shao, Y.; Xiao, Z.; Bi, C.; Yuan, Y.; Huang, J. Origin and elimination of photocurrent hysteresis by fullerene passivation in CH₃NH₃PbI₃ planar heterojunction solar cells. *Nat. Commun.* **2014**, *5*, 5784. [CrossRef]
61. Choi, S.; Shin, W.; Oh, J.; Ryu, M.-Y.; Lee, H. Enhancement in Device Performance of Perovskite Solar Cells via Annealing of PCBM Electron Transport Layer. *Appl. Sci. Conver. Technol.* **2022**, *31*, 167–170. [CrossRef]
62. Mehdi, H.; Selmi, O.; Mhamdi, A.; Bouazizi, A. Effect of annealing treatment of PC60BM layer on inverted perovskite solar cells. *J. Mater. Sci. Mater. Electron.* **2022**, *33*, 5351–5358. [CrossRef]
63. Liu, Y.; Shin, I.; Hwang, I.-W.; Kim, S.; Lee, J.; Yang, M.-S.; Jung, Y.K.; Jang, J.-W.; Jeong, J.H.; Park, S.H.; et al. Single-Crystal-like Perovskite for High-Performance Solar Cells Using the Effective Merged Annealing Method. *ACS Appl. Mater. Interfaces* **2017**, *9*, 12382–12390. [CrossRef] [PubMed]
64. Wu, H.; Lian, X.; Li, J.; Zhang, Y.; Zhou, G.; Wen, X.; Xie, Z.; Zhu, H.; Wu, G.; Chen, H. Merged interface construction toward ultra-low V_{oc} loss in inverted two-dimensional Dion–Jacobson perovskite solar cells with efficiency over 18%. *J. Mater. Chem. A* **2021**, *9*, 12566–12573. [CrossRef]
65. Lian, X.; Wu, H.; Zuo, L.; Zhou, G.; Wen, X.; Zhang, Y.; Wu, G.; Xie, Z.; Zhu, H.; Chen, H. Stable Quasi-2D Perovskite Solar Cells with Efficiency over 18% Enabled by Heat–Light Co-Treatment. *Adv. Funct. Mater.* **2020**, *30*, 2004188. [CrossRef]

66. Zhou, L.; Chang, J.; Liu, Z.; Sun, X.; Lin, Z.; Chen, D.; Zhang, C.; Zhang, J.; Hao, Y. Enhanced Planar Perovskite Solar Cells Efficiency and Stability Using Perovskite/PCBM Heterojunction through One-Step Formation. *Nanoscale* **2018**, *10*, 3053–3059. [[CrossRef](#)]
67. Butsriruk, K.; Passokorn, P.; Taychatanapat, T.; Chatraphorn, S. Surface treatment of PTAA hole transport layer for inverted perovskite solar cells. *J. Phys. Conf. Ser.* **2023**, *2431*, 012045. [[CrossRef](#)]
68. Calió, L.; Kazim, S.; Grätzel, M.; Ahmad, S. Hole-Transport Materials for Perovskite Solar Cells. *Angew Chem. Int. Ed.* **2016**, *55*, 14522–14545. [[CrossRef](#)] [[PubMed](#)]
69. Jiménez-González, A.E.; Cambray, J.G. Deposition of NiO_x thin films by sol–gel technique. *Surf. Eng.* **2000**, *16*, 73–76. [[CrossRef](#)]
70. Ghodsi, F.E.; Khayatiyan, S.A. Preparation and Determination of Optical Properties of NiO Thin Films Deposited by Dip Coating Technique. *Surf. Rev. Lett.* **2007**, *14*, 219–224. [[CrossRef](#)]
71. Patil, V.P.; Pawar, S.; Chougule, M.; Godse, P.; Sakhare, R.; Sen, S.; Joshi, P. Effect of Annealing on Structural, Morphological, Electrical and Optical Studies of Nickel Oxide Thin Films. *J. Surf. Eng. Mater. Adv. Technol.* **2011**, *1*, 35–41. [[CrossRef](#)]
72. Nalage, S.R.; Chougule, M.A.; Sen, S.; Joshi, P.B.; Patil, V.B. Sol–gel synthesis of nickel oxide thin films and their characterization. *Thin Solid Films* **2012**, *520*, 4835–4840. [[CrossRef](#)]
73. Zorkipli, N.N.M.; Kaus, N.H.M.; Mohamad, A.A. Synthesis of NiO Nanoparticles through Sol-gel Method. *Procedia Chem.* **2016**, *19*, 626–631. [[CrossRef](#)]
74. Kayani, Z.N.; Butt, M.Z.; Riaz, S.; Naseem, S. Synthesis of NiO nanoparticles by sol-gel technique. *Mater. Sci.* **2018**, *36*, 547–552. [[CrossRef](#)]
75. Yin, X.; Guo, Y.; Xie, H.; Que, W.; Kong, L.B. Nickel Oxide as Efficient Hole Transport Materials for Perovskite Solar Cells. *Sol. RRL* **2019**, *3*, 1900001. [[CrossRef](#)]
76. Park, I.J.; Kang, G.; Park, M.A.; Kim, J.S.; Seo, S.W.; Kim, D.H.; Zhu, K.; Park, T.; Kim, J.Y. Highly Efficient and Uniform 1 cm² Perovskite Solar Cells with an Electrochemically Deposited NiO_x Hole-Extraction Layer. *ChemSusChem* **2017**, *10*, 2660–2667. [[CrossRef](#)] [[PubMed](#)]
77. Kim, H.-S.; Lee, C.-R.; Im, J.-H.; Lee, K.-B.; Moehl, T.; Marchioro, A.; Moon, S.-J.; Humphry-Baker, R.; Yum, J.-H.; Moser, J.E.; et al. Lead Iodide Perovskite Sensitized All-Solid-State Submicron Thin Film Mesoscopic Solar Cell with Efficiency Exceeding 9%. *Sci. Rep.* **2012**, *2*, 591. [[CrossRef](#)]
78. Macdonald, T.J.; Batmunkh, M.; Lin, C.-T.; Kim, J.; Tune, D.D.; Ambroz, F.; Li, X.; Xu, S.; Sol, C.; Papakonstantinou, I.; et al. Origin of Performance Enhancement in TiO₂-Carbon Nanotube Composite Perovskite Solar Cells. *Small Methods* **2019**, *3*, 1900164. [[CrossRef](#)]
79. Fang, Y.; Wang, X.; Wang, Q.; Huang, J.; Wu, T. Impact of annealing on spiro-OMeTAD and corresponding solid-state dye sensitized solar cells: Impact of annealing on spiro-OMeTAD. *Phys. Status Solidi A* **2014**, *211*, 2809–2816. [[CrossRef](#)]
80. Rombach, F.M.; Haque, S.A.; Macdonald, T.J. Lessons learned from spiro-OMeTAD and PTAA in perovskite solar cells. *Energy Environ. Sci.* **2021**, *14*, 5161–5190. [[CrossRef](#)]
81. Zhao, X.; Kim, H.-S.; Seo, J.-Y.; Park, N.-G. Effect of Selective Contacts on the Thermal Stability of Perovskite Solar Cells. *ACS Appl. Mater. Interfaces* **2017**, *9*, 7148–7153. [[CrossRef](#)]
82. Malinauskas, T.; Tomkute-Luksiene, D.; Sens, R.; Daskeviciene, M.; Send, R.; Wonneberger, H.; Jankauskas, V.; Bruder, I.; Getautis, V. Enhancing Thermal Stability and Lifetime of Solid-State Dye-Sensitized Solar Cells via Molecular Engineering of the Hole-Transporting Material Spiro-OMeTAD. *ACS Appl. Mater. Interfaces* **2015**, *7*, 11107–11116. [[CrossRef](#)]
83. Mesquita, I.; Andrade, L.; Mendes, A. Temperature Impact on Perovskite Solar Cells Under Operation. *ChemSusChem* **2019**, *12*, 2186–2194. [[CrossRef](#)]
84. Bailie, C.D.; Unger, E.L.; Zakeeruddin, S.M.; Grätzel, M.; McGehee, M.D. Melt-infiltration of spiro-OMeTAD and thermal instability of solid-state dye-sensitized solar cells. *Phys. Chem. Chem. Phys.* **2014**, *16*, 4864. [[CrossRef](#)]
85. Wang, S.; Sina, M.; Parikh, P.; Uekert, T.; Shahbazian, B.; Devaraj, A.; Meng, Y.S. Role of 4-tert-Butylpyridine as a Hole Transport Layer Morphological Controller in Perovskite Solar Cells. *Nano Lett.* **2016**, *16*, 5594–5600. [[CrossRef](#)] [[PubMed](#)]
86. Kasparavicius, E.; Magomedov, A.; Malinauskas, T.; Getautis, V. Long-Term Stability of the Oxidized Hole-Transporting Materials used in Perovskite Solar Cells. *Chem. A Eur. J.* **2018**, *24*, 9910–9918. [[CrossRef](#)] [[PubMed](#)]
87. Heo, J.H.; Im, S.H.; Noh, J.H.; Mandal, T.N.; Lim, C.-S.; Chang, J.A.; Lee, Y.H.; Kim, H.; Sarkar, A.; Nazeeruddin, M.K.; et al. Efficient inorganic–organic hybrid heterojunction solar cells containing perovskite compound and polymeric hole conductors. *Nat. Photon.* **2013**, *7*, 486–491. [[CrossRef](#)]
88. Ko, Y.; Kim, Y.; Lee, C.; Kim, Y.; Jun, Y. Investigation of Hole-Transporting Poly(triarylamine) on Aggregation and Charge Transport for Hysteresisless Scalable Planar Perovskite Solar Cells. *ACS Appl. Mater. Interfaces* **2018**, *10*, 11633–11641. [[CrossRef](#)]
89. Sharif, R.; Khalid, A.; Ahmad, S.W.; Rehman, A.; Qutab, H.G.; Akhtar, H.H.; Mahmood, K.; Afzal, S.; Saleem, F. A comprehensive review of the current progresses and material advances in perovskite solar cells. *Nanoscale Adv.* **2023**, *5*, 3803–3833. [[CrossRef](#)]
90. Bruening, K.; Tassone, C.J. Antisolvent processing of lead halide perovskite thin films studied by in situ X-ray diffraction. *J. Mater. Chem. A* **2018**, *6*, 18865–18870. [[CrossRef](#)]
91. Chen, S.; Xiao, X.; Chen, B.; Kelly, L.L.; Zhao, J.; Lin, Y.; Toney, M.F.; Huang, J. Crystallization in one-step solution deposition of perovskite films: Upward or downward? *Sci. Adv.* **2021**, *7*, eabb2412. [[CrossRef](#)] [[PubMed](#)]
92. Barrows, A.T.; Lilliu, S.; Pearson, A.J.; Babonneau, D.; Dunbar, A.D.F.; Lidzey, D.G. Monitoring the Formation of a CH₃ NH₃ PbI_{3-x} Cl_x Perovskite during Thermal Annealing Using X-Ray Scattering. *Adv. Funct. Mater.* **2016**, *26*, 4934–4942. [[CrossRef](#)]

93. Oyewole, D.O.; Koech, R.K.; Ichwani, R.; Ahmed, R.; Hinojosa Tamayo, J.; Adeniji, S.A.; Cromwell, J.; Colin Ulloa, E.; Oyewole, O.K.; Agyei-Tuffour, B.; et al. Annealing effects on interdiffusion in layered FA-rich perovskite solar cells. *AIP Adv.* **2021**, *11*, 065327. [[CrossRef](#)]
94. Ali Akhavan Kazemi, M.; Jamali, A.; Sauvage, F. A Holistic Study on the Effect of Annealing Temperature and Time on CH₃NH₃PbI₃-Based Perovskite Solar Cell Characteristics. *Front. Energy Res.* **2021**, *9*, 732886. [[CrossRef](#)]
95. Chiang, C.-H.; Tseng, Z.-L.; Wu, C.-G. Planar heterojunction perovskite/PC₇₁ BM solar cells with enhanced open-circuit voltage via a (2/1)-step spin-coating process. *J. Mater. Chem. A* **2014**, *2*, 15897–15903. [[CrossRef](#)]
96. Jeon, N.J.; Noh, J.H.; Yang, W.S.; Kim, Y.C.; Ryu, S.; Seo, J.; Seok, S.I. Compositional engineering of perovskite materials for high-performance solar cells. *Nature* **2015**, *517*, 476–480. [[CrossRef](#)] [[PubMed](#)]
97. Zhao, X.; Liu, T.; Kaplan, A.B.; Yao, C.; Loo, Y.-L. Accessing Highly Oriented Two-Dimensional Perovskite Films via Solvent-Vapor Annealing for Efficient and Stable Solar Cells. *Nano Lett.* **2020**, *20*, 8880–8889. [[CrossRef](#)] [[PubMed](#)]
98. Sã, S. Flash infrared annealing as a cost-effective and low environmental impact processing method for planar perovskite solar cells. *Mater. Today* **2019**, *31*, 39–46.
99. Lavery, B.W.; Kumari, S.; Konermann, H.; Draper, G.L.; Spurgeon, J.; Druffel, T. Intense Pulsed Light Sintering of CH₃NH₃PbI₃ Solar Cells. *ACS Appl. Mater. Interfaces* **2016**, *8*, 8419–8426. [[CrossRef](#)]
100. Zheng, Z.-H.; Lan, H.-B.; Su, Z.-H.; Peng, H.-X.; Luo, J.-T.; Liang, G.-X.; Fan, P. Single Source Thermal Evaporation of Two-dimensional Perovskite Thin Films for Photovoltaic Applications. *Sci. Rep.* **2019**, *9*, 17422. [[CrossRef](#)]
101. Li, B.; Jiu, T.; Kuang, C.; Ma, S.; Chen, Q.; Li, X.; Fang, J. Chlorobenzene vapor assistant annealing method for fabricating high quality perovskite films. *Org. Electron.* **2016**, *34*, 97–103. [[CrossRef](#)]
102. Li, Y.; Chen, J.; Cai, P.; Wen, Z. An electrochemically neutralized energy-assisted low-cost acid-alkaline electrolyzer for energy-saving electrolysis hydrogen generation. *J. Mater. Chem. A* **2018**, *6*, 4948–4954. [[CrossRef](#)]
103. You, P.; Li, G.; Tang, G.; Cao, J.; Yan, F. Ultrafast laser-annealing of perovskite films for efficient perovskite solar cells. *Energy Environ. Sci.* **2020**, *13*, 1187–1196. [[CrossRef](#)]
104. Ghahremani, A.H.; Martin, B.; Gupta, A.; Bahadur, J.; Ankireddy, K.; Druffel, T. Rapid fabrication of perovskite solar cells through intense pulse light annealing of SnO₂ and triple cation perovskite thin films. *Mater. Des.* **2020**, *185*, 108237. [[CrossRef](#)]
105. Chen, Q.; Ma, T.; Wang, F.; Liu, Y.; Liu, S.; Wang, J.; Cheng, Z.; Chang, Q.; Yang, R.; Huang, W.; et al. Rapid Microwave-Annealing Process of Hybrid Perovskites to Eliminate Miscellaneous Phase for High Performance Photovoltaics. *Adv. Sci.* **2020**, *7*, 2000480. [[CrossRef](#)] [[PubMed](#)]
106. Wang, K.-L.; Zhang, C.-C.; Jiang, Y.-R.; Liu, H.-R.; Li, X.-M.; Jain, S.M.; Ma, H. High-quality perovskite films *via* post-annealing microwave treatment. *New J. Chem.* **2019**, *43*, 9338–9344. [[CrossRef](#)]
107. Hua, J.; Deng, X.; Niu, C.; Huang, F.; Peng, Y.; Li, W.; Ku, Z.; Cheng, Y. A pressure-assisted annealing method for high quality CsPbBr₃ film deposited by sequential thermal evaporation. *RSC Adv.* **2020**, *10*, 8905–8909. [[CrossRef](#)]
108. Martin, B.; Yang, M.; Bramante, R.C.; Amerling, E.; Gupta, G.; Van Hest, M.F.A.M.; Druffel, T. Fabrication of flexible perovskite solar cells via rapid thermal annealing. *Mater. Lett.* **2020**, *276*, 128215. [[CrossRef](#)]
109. Dong, G.; Yang, Y.; Sheng, L.; Xia, D.; Su, T.; Fan, R.; Shi, Y.; Wang, J. Inverted thermal annealing of perovskite films: A method for enhancing photovoltaic device efficiency. *RSC Adv.* **2016**, *6*, 44034–44040. [[CrossRef](#)]
110. Li, N.; Niu, X.; Li, L.; Wang, H.; Huang, Z.; Zhang, Y.; Chen, Y.; Zhang, X.; Zhu, C.; Zai, H.; et al. Liquid medium annealing for fabricating durable perovskite solar cells with improved reproducibility. *Science* **2021**, *373*, 561–567. [[CrossRef](#)]
111. Eze, V.O.; Seike, Y.; Mori, T. Synergistic Effect of Additive and Solvent Vapor Annealing on the Enhancement of MAPbI₃ Perovskite Solar Cells Fabricated in Ambient Air. *ACS Appl. Mater. Interfaces* **2020**, *12*, 46837–46845. [[CrossRef](#)]
112. Sun, X.; Zhang, C.; Chang, J.; Yang, H.; Xi, H.; Lu, G.; Chen, D.; Lin, Z.; Lu, X.; Zhang, J.; et al. Mixed-solvent-vapor annealing of perovskite for photovoltaic device efficiency enhancement. *Nano Energy* **2016**, *28*, 417–425. [[CrossRef](#)]
113. Chin, S.-H.; Choi, J.W.; Woo, H.C.; Kim, J.H.; Lee, H.S.; Lee, C.-L. Realizing a highly luminescent perovskite thin film by controlling the grain size and crystallinity through solvent vapour annealing. *Nanoscale* **2019**, *11*, 5861–5867. [[CrossRef](#)] [[PubMed](#)]
114. Yuan, B.; Zhao, S.; Xu, Z.; Song, D.; Qiao, B.; Li, Y.; Qin, Z.; Meng, J.; Xu, X. Improving the photovoltaic performance of planar heterojunction perovskite solar cells by mixed solvent vapor treatment. *RSC Adv.* **2018**, *8*, 11574–11579. [[CrossRef](#)] [[PubMed](#)]
115. Luo, J.; Qiu, R.Z.; Yang, Z.S.; Wang, Y.X.; Zhang, Q.F. Mechanism and effect of γ -butyrolactone solvent vapor post-annealing on the performance of a mesoporous perovskite solar cell. *RSC Adv.* **2018**, *8*, 724–731. [[CrossRef](#)]
116. Serafini, P.; Boix, P.P.; Barea, E.M.; Edvinson, T.; Sánchez, S.; Mora-Seró, I. Photonic Processing of MAPbI₃ Films by Flash Annealing and Rapid Growth for High-Performance Perovskite Solar Cells. *Solar RRL* **2022**, *6*, 2200641. [[CrossRef](#)]
117. Sanchez, S.; Hua, X.; Phung, N.; Steiner, U.; Abate, A. Flash Infrared Annealing for Antisolvent-Free Highly Efficient Perovskite Solar Cells. *Adv. Energy Mater.* **2018**, *8*, 1702915. [[CrossRef](#)]
118. Sanchez, S.; Christoph, N.; Grobety, B.; Phung, N.; Steiner, U.; Saliba, M.; Abate, A. Efficient and Stable Inorganic Perovskite Solar Cells Manufactured by Pulsed Flash Infrared Annealing. *Adv. Energy Mater.* **2018**, *8*, 1802060. [[CrossRef](#)]
119. Murugadoss, G.; Thangamuthu, R.; Rajesh Kumar, M.; Sakkarapalayam Murugesan, S.K.; Prabu, V. Air free fast solution annealing method for perovskite solar cells. *Mater. Lett.* **2017**, *205*, 130–133. [[CrossRef](#)]
120. Zhi, L.; Li, Y.; Cao, X.; Li, Y.; Cui, X.; Ci, L.; Wei, J. Dissolution and recrystallization of perovskite induced by N-methyl-2-pyrrolidone in a closed steam annealing method. *J. Energy Chem.* **2019**, *30*, 78–83. [[CrossRef](#)]

121. Francisco-López, A.; Charles, B.; Weber, O.J.; Alonso, M.I.; Garriga, M.; Campoy-Quiles, M.; Weller, M.T.; Goñi, A.R. Equal Footing of Thermal Expansion and Electron–Phonon Interaction in the Temperature Dependence of Lead Halide Perovskite Band Gaps. *J. Phys. Chem. Lett.* **2019**, *10*, 2971–2977. [[CrossRef](#)] [[PubMed](#)]
122. Aydin, E.; Allen, T.G.; De Bastiani, M.; Xu, L.; Ávila, J.; Salvador, M.; Van Kerschaver, E.; De Wolf, S. Interplay between temperature and bandgap energies on the outdoor performance of perovskite/silicon tandem solar cells. *Nat. Energy* **2020**, *5*, 851–859. [[CrossRef](#)]
123. Yuan, Y.; Chae, J.; Shao, Y.; Wang, Q.; Xiao, Z.; Centrone, A.; Huang, J. Photovoltaic Switching Mechanism in Lateral Structure Hybrid Perovskite Solar Cells. *Adv. Energy Mater.* **2015**, *5*, 1500615. [[CrossRef](#)]
124. Wu, X.; Wu, B.; Zhu, Z.; Tayyab, M.; Gao, D. Importance and Advancement of Modification Engineering in Perovskite Solar Cells. *Solar RRL* **2022**, *6*, 2200171. [[CrossRef](#)]
125. Chen, Z.; Yang, Z.; Du, S.; Lin, D.; Zhang, F.; Zeng, Y.; Liu, G.; Nie, Z.; Ma, L. Thermal stability and decomposition kinetics of mixed-cation halide perovskites. *Phys. Chem. Chem. Phys.* **2023**, *25*, 32966–32971. [[CrossRef](#)]
126. Bush, K.A.; Palmstrom, A.F.; Yu, Z.J.; Boccard, M.; Cheacharoen, R.; Mailoa, J.P.; McMeekin, D.P.; Hoyer, R.L.Z.; Bailie, C.D.; Leijtens, T.; et al. 23.6%-efficient monolithic perovskite/silicon tandem solar cells with improved stability. *Nat. Energy* **2017**, *2*, 17009. [[CrossRef](#)]
127. Bush, K.A.; Bailie, C.D.; Chen, Y.; Bowring, A.R.; Wang, W.; Ma, W.; Leijtens, T.; Moghadam, F.; McGehee, M.D. Thermal and Environmental Stability of Semi-Transparent Perovskite Solar Cells for Tandems Enabled by a Solution-Processed Nanoparticle Buffer Layer and Sputtered ITO Electrode. *Adv. Mater.* **2016**, *28*, 3937–3943. [[CrossRef](#)]
128. Fu, F.; Feurer, T.; Weiss, T.P.; Pisoni, S.; Avancini, E.; Andres, C.; Buecheler, S.; Tiwari, A.N. High-efficiency inverted semi-transparent planar perovskite solar cells in substrate configuration. *Nat. Energy* **2016**, *2*, 16190. [[CrossRef](#)]
129. Mariotti, S.; Jäger, K.; Diederich, M.; Härtel, M.S.; Li, B.; Sveinbjörnsson, K.; Kajari-Schröder, S.; Peibst, R.; Albrecht, S.; Korte, L.; et al. Monolithic Perovskite/Silicon Tandem Solar Cells Fabricated Using Industrial p-Type Polycrystalline Silicon on Oxide/Passivated Emitter and Rear Cell Silicon Bottom Cell Technology. *Solar RRL* **2022**, *6*, 2101066. [[CrossRef](#)]
130. Kuwano, K.; Ashok, S. Investigation of sputtered indium-tin oxide/silicon interfaces: Ion damage, hydrogen passivation and low-temperature anneal. *Appl. Surf. Sci.* **1997**, *117*, 629–633. [[CrossRef](#)]
131. Liu, J.; De Bastiani, M.; Aydin, E.; Harrison, G.T.; Gao, Y.; Pradhan, R.R.; Eswaran, M.K.; Mandal, M.; Yan, W.; Seitkhan, A.; et al. Efficient and stable perovskite-silicon tandem solar cells through contact displacement by MgF_x. *Science* **2022**, *377*, 302–306. [[CrossRef](#)] [[PubMed](#)]
132. Ono, L.K.; Raga, S.R.; Wang, S.; Kato, Y.; Qi, Y. Temperature-dependent hysteresis effects in perovskite-based solar cells. *J. Mater. Chem. A* **2015**, *3*, 9074–9080. [[CrossRef](#)]
133. Ishii, T.; Otani, K.; Takashima, T.; Kawai, S. Estimation of the maximum power temperature coefficients of PV modules at different time scales. *Sol. Energy Mater. Sol. Cells* **2011**, *95*, 386–389. [[CrossRef](#)]
134. Liu, S.H.; Simburger, E.J.; Matsumoto, J.; Garcia, A.; Ross, J.; Nocerino, J. Evaluation of thin-film solar cell temperature coefficients for space applications. *Prog. Photovolt.* **2005**, *13*, 149–156. [[CrossRef](#)]
135. Habisreutinger, S.N.; Leijtens, T.; Eperon, G.E.; Stranks, S.D.; Nicholas, R.J.; Snaith, H.J. Carbon Nanotube/Polymer Composites as a Highly Stable Hole Collection Layer in Perovskite Solar Cells. *Nano Lett.* **2014**, *14*, 5561–5568. [[CrossRef](#)] [[PubMed](#)]
136. Ava, T.T.; Al Mamun, A.; Marsillac, S.; Namkoong, G. A Review: Thermal Stability of Methylammonium Lead Halide Based Perovskite Solar Cells. *Appl. Sci.* **2019**, *9*, 188. [[CrossRef](#)]
137. Bruno, A.; Cortecchia, D.; Chin, X.Y.; Fu, K.; Boix, P.P.; Mhaisalkar, S.; Soci, C. Temperature and Electrical Poling Effects on Ionic Motion in MAPbI₃ Photovoltaic Cells. *Adv. Energy Mater.* **2017**, *7*, 1700265. [[CrossRef](#)]
138. Yuan, Y.; Huang, J. Ion Migration in Organometal Trihalide Perovskite and Its Impact on Photovoltaic Efficiency and Stability. *Acc. Chem. Res.* **2016**, *49*, 286–293. [[CrossRef](#)]
139. Jošt, M.; Lipovšek, B.; Glažar, B.; Al-Ashouri, A.; Brecl, K.; Matič, G.; Magomedov, A.; Getautis, V.; Topič, M.; Albrecht, S. Perovskite Solar Cells go Outdoors: Field Testing and Temperature Effects on Energy Yield. *Adv. Energy Mater.* **2020**, *10*, 2000454. [[CrossRef](#)]
140. Bhandari, S.; Mallick, T.K.; Sundaram, S. Enlightening the temperature coefficient of triple mesoscopic CH₃NH₃Pb_{1–x}Cl_x/NiO and double mesoscopic CsFAMAPb_{1–x}Br_x/CuSCN carbon perovskite solar cells. *J. Phys. Energy* **2023**, *5*, 025006. [[CrossRef](#)]
141. Khenkin, M.V.; Katz, E.A.; Abate, A.; Bardizza, G.; Berry, J.J.; Brabec, C.; Brunetti, F.; Bulović, V.; Burlingame, Q.; Di Carlo, A.; et al. Consensus statement for stability assessment and reporting for perovskite photovoltaics based on ISOS procedures. *Nat. Energy* **2020**, *5*, 35–49. [[CrossRef](#)]

Disclaimer/Publisher’s Note: The statements, opinions and data contained in all publications are solely those of the individual author(s) and contributor(s) and not of MDPI and/or the editor(s). MDPI and/or the editor(s) disclaim responsibility for any injury to people or property resulting from any ideas, methods, instructions or products referred to in the content.